Journal of Rock Mechanics and Geotechnical Engineering 15 (2023) 2423–2440

Contents lists available at ScienceDirect

Journal of Rock Mechanics and Geotechnical Engineering

journal homepage: www.jrmge.cn

Full Length Article

Influence of variables related to soil weathering on the geomechanical performance of tropical soils

Rodrigo Cesar Pierozan [a,*], Gregorio Luís Silva Araújo [b], Ennio Marques Palmeira [b], Celso Romanel [c]

[a] Department of Civil Engineering, Federal Institute of Education, Science, and Technology of Rondonia, Porto Velho, RO, Brazil
[b] Department of Civil and Environmental Engineering, University of Brasilia, Brasilia, DF, Brazil
[c] Department of Civil and Environmental Engineering, Pontifical Catholic University of Rio de Janeiro, Rio de Janeiro, RJ, Brazil

ARTICLE INFO

Article history:
Received 11 July 2022
Received in revised form
24 February 2023
Accepted 11 April 2023
Available online 19 May 2023

Keywords:
Sesquioxides-silica ratio
Tropical soils
Sand-silt mixtures
Lateritic soil
Reinforced soil walls

ABSTRACT

This paper presents an experimental and analytical investigation of the influence of variables related to soil weathering on the geomechanical performance of sand-silt mixtures containing lateritic soils, i.e. intensely weathered tropical soils with the influence of interparticle bonding. The sand-silt mixtures containing different relative proportions between uniform sand and lateritic soil were produced, and geomechanical soil characterization tests were performed. Based on the results, a transition from a primarily coarse-to a fine-grained prevailing soil structure was found to cause considerable impact on the geomechanical performance of these soils, as evidenced by design variables related to soil mineralogy and size distribution characteristics. Specifically, fines contents of both individual soil particles and soil aggregations were found to correlate with experimental results, while the relative proportion between sesquioxides (aluminum, and iron oxides), and silica, i.e. sesquioxide-silica ratios (SSR^{-1}), facilitated estimates concerning changes in geomechanical performance. Finally, the application of the sand-silt mixtures containing lateritic soil on soil walls reinforced with polymeric strips was also evaluated, further emphasizing the potential advantages of adopting variables related to soil weathering on design guidelines concerning tropical soils.

1. Introduction

Granular aggregates, such as clean uniform sands and gravels, have often been the preferred source of construction materials for use as structural fills in reinforced soil walls due to the overall adequate range of internal shear strength, compressibility, and drainage capabilities presented by these materials (e.g. Elias et al., 2001; BS EN 14475, 2006; NF P94-270, 2009; EBGEO, 2011), which can also translate into enhanced soil-reinforcement interaction mechanisms (e.g. Schlosser and Bastick, 1991; Lajevardi et al., 2013; Abdi and Mirzaeifar, 2017; Pierozan et al., 2022). Nonetheless, in recent decades, concerns related to the exploitation of natural aggregates, prospects of limited availability, and correlated costs, have prompted geotechnical engineers to investigate feasible alternative construction materials, such as fine-grained cohesive soils (e.g. Abd and Utili, 2017; Chen et al., 2018; Altay et al., 2019).

Lateritic soils are a category of fine-grained residual soils typically found in humid tropical and subtropical regions, such as sizeable areas of Latin America, Africa, Asia, and Oceania, in which year-round intense climate conditions are prone to develop (e.g. Catt, 1990; Benatti and Miguel, 2013; Tran et al., 2019). For instance, typical features of such climate conditions include the occurrence of rainy seasons followed by intense droughts, large precipitation events, intense solar heating, and large daily and seasonal temperature oscillations, which favor the continued degradation of parent materials by oxidation reactions and chemical leaching processes. These conditions may lead to the accumulation of hydrated iron and aluminum oxides (sesquioxides) between the particles formed by the more stable minerals, such as quartz, which ultimately lead to the development of water-stable micro-aggregations (e.g. Leroueil and Vaughan, 1990; Mahalinga-Iyer and Williams, 1994; Morandini and Leite, 2015; Ng et al., 2019).

* Corresponding author.
E-mail address: rodrigo.pierozan@ifro.edu.br (R.C. Pierozan).
Peer review under responsibility of Institute of Rock and Soil Mechanics, Chinese Academy of Sciences.

https://doi.org/10.1016/j.jrmge.2023.04.005

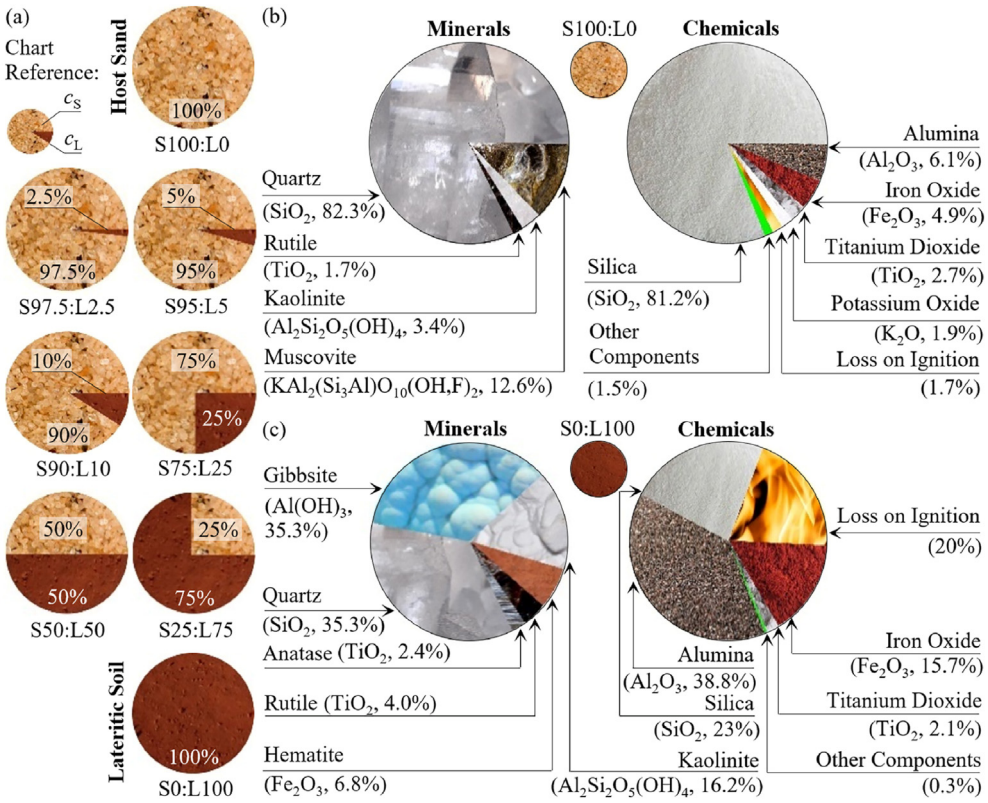

Fig. 1. Tested soils and relevant mineral and chemical characteristics: (a) Schematic representation of the studied sand-silt mixtures, (b) Results associated with the host sand (S100:L0), and (c) Results associated with the lateritic soil (S0:L100).

Given the particularities inherent to the formation of lateritic soils, a distinct geomechanical behavior, relative to their counterparts found in temperate regions, is expected (Gidigasu, 1972). Specifically, the sesquioxides coating may reduce the susceptibility of the clay mineral to absorb water, causing a decrease in plasticity, compared to the fine-grained soils found in temperate regions (e.g. Townsend et al., 1971; Mohamed and Paleologos, 2018). However, it can provide an additional component of internal shear strength, i.e. the interparticle bonding, comparing with conventional fine-grained soils. These characteristics have favored the development of pavement (e.g. Carvalho et al., 2015; Mengue et al., 2018; Freitas et al., 2020; Lima et al., 2021) and railway (e.g. Guimarães et al., 2021) structures on a broad range of lateritic soil foundations.

Variables related to the soil weathering are often disregarded as input arguments in design guidelines, despite the influence of the mineral composition on the geomechanical responses of lateritic soils. For instance, only few investigations may be found in the technical literature concerning the improvement of lateritic soils for use as structural fills (e.g. Okagbue and Onyeobi, 1999; Latifi et al., 2016, 2017; Anggraini et al., 2017; Araujo et al., 2021), leading to potential design difficulties and misconceptions when dealing with tropical soils.

This investigation focuses on evaluating the influence of the variables that are deemed to better represent the geomechanical behavior of the sand-silt mixtures containing lateritic soils, such as the sesquioxide-silica ratios (SSR^{-1}), and the contents of soil aggregations (FC_{aggreg}), which could be implemented into analytical tools to predict the geomechanical behavior of these unconventional fill materials. The experimental component of this research included a wide range of soil geomechanical characterization tests on the sand-silt mixtures with varying lateritic soil contents. Finally, based on the insight provided by this survey, variables related to soil weathering were also evaluated from the perspective of reinforced soil structures, following pullout tests on polymeric strips.

2. Tested soils

Natural sand, extracted from a fluvial deposit at Rio das Almas (State of Goias, Brazil), and an intensely weathered tropical soil (lateritic soil, as in Santos et al., 2013), collected at the Experimental Field of the University of Brasilia Geotechnical Engineering Graduate Program (Federal District, Brazil), were employed in this research. Sample preparation followed the procedures in ASTM D421-85 (2007), with particular attention to the removal of particles with dimensions smaller than 0.075 mm from the natural sand, and the removal of particles larger than 2 mm from both soils.

A schematic representation of the mass fractions relative to the clean uniform sand and the lateritic soil used to prepare the sand-silt mixtures is shown in Fig. 1a, with the adopted nomenclature indicated as S(c_S):L(c_L), i.e. acronyms S and L refer to host sand and lateritic soil, respectively; and c_S and c_L indicate their respective mass fractions:

$$c_S = \frac{m_S}{m_S + m_L} \tag{1}$$

$$c_L = 1 - c_S \tag{2}$$

where m_S and m_L are the dry masses of S and L, respectively.

Based on Fig. 1a, lateritic soil mass fractions (c_L) ranging from 0 (S100:L0) to 1 (S0:L100) were evaluated in this research, encompassing eight mass fractions. It should be noted that the total range of c_L was divided into four quarters, i.e. ranging from 0 to 0.25

(S75:L25), 0.25 to 0.5 (S50:L50), 0.5 to 0.75 (S25:L75), and 0.75 to 1, with additional data points established in the $0 < c_L < 0.25$ range (i.e. 0.025 (S97.5:L2.5), 0.05 (S95:L5), and 0.1 (S90:L10)). This is because identifying the transition from a primarily coarse-to a fine-grained prevailing soil structure was one of the main objectives of this work, which usually develops under relatively low cohesive soil mass fractions.

A summary of the values attributed to geomechanical fill properties is presented in Table 1. Details on testing procedures and data analysis are as follows.

2.1. Mineral and chemical composition

The X-ray diffraction (XRD) technique was employed to provide insight into the mineral composition of the tested soils, while the X-ray fluorescent spectrometry (XRF) technique facilitated the evaluation of the chemical components. Results are shown in Fig. 1b and c considering the host sand (S100:L0) and the lateritic soil (S0:L100), respectively. In terms of minerals, quartz was a primary component of both soils (with equivalent mass fractions of 82.3% and 35.3% for the host sand (S100:L0) and lateritic soil (S0:L100), respectively), while the lateritic soil (S0:L100) also presented a significant share of gibbsite (35.3%), kaolinite (16.2%), and hematite (6.8%). It should be noted that kaolinite was the prevalent clay mineral found in the lateritic soil (S0:L100), while the relatively large share of gibbsite and hematite could be attributed to the sesquioxide coating that was a characteristic of intensely weathered soils (e.g. Araujo et al., 2009; Rezende et al., 2015; Mohamed and Paleologos, 2018).

Overall, based on Fig. 1b and c, chemical testing results agreed with the mineralogical components. Specifically, silica (81.2%) was the major chemical component of the host sand (S100:L0), thus qualifying this material as silica sand (e.g. Klein and Hurlbut, 1993). On the other hand, the major components attributed to the lateritic soil (S0:100) included a considerable share of sesquioxides (alumina (38.8%) and iron oxide (15.7%)), besides silica (23%). It should be emphasized that, when it comes to the lateritic soil (S0:100), the presence of silica could be attributed to a fraction of the lateritic soil which had been previously subjected to early stages of weathering (i.e. a coarse-grained soil skeleton). Conversely, the relatively large share of sesquioxides soil fractions is indicative of intense weathering conditions, which could ultimately influence the overall geomechanical behavior of the soil.

The variables related to the mineralogical composition are not frequently considered as the input arguments in analytical models to predict geomechanical responses (Zhang et al., 2020), even though their influence could be particularly relevant when dealing with intensely weathered tropical soils, i.e. the lateritic soil employed in this research. Previous investigations have considered establishing a silica-sesquioxide ratio (*SSR*) to distinguish tropical soils based on major chemical components (Catt, 1990):

$$SSR = \frac{\frac{c_{SiO_2}}{60}}{\frac{c_{Al_2O_3}}{102} + \frac{c_{Fe_2O_3}}{160}} \tag{3}$$

where *SSR* denotes the silica-sesquioxides ratio; and c_{SiO_2}, $c_{Al_2O_3}$ and $c_{Fe_2O_3}$ represent the percentages of chemical components silica, alumina and iron oxide, respectively.

Based on Eq. (3), *SSR* values ranging from 14.97 (S100:L0) to 0.8 (S0:L100) were attributed to the soils investigated in this research, as summarized in Table 1. Specifically, the *SSR* value attributed to the lateritic soil (S0:L100), i.e. 14.97, agrees with intensely weathered soils, as in the soil classification proposed by Catt (1990).

Despite the usefulness of *SSR* when it comes to clustering tropical soils into different categories (e.g. Gidigasu, 1972; Catt, 1990), it should be underlined that the values assumed by *SSR* are inversely related to a number of variables related to the geomechanical behavior of soils. For instance, soil parameters associated with water percolation, compressibility, and plasticity are inversely proportional to *SSR*. Since the focus of the paper is to evaluate the impact of the lateritic soil on the geomechanical performance of fill materials, the consideration of sesquioxides-silica

Table 1
Geomechanical soil characteristics evaluated in this research.

Geotechnical properties	S100:L0	S97.5:L2.5	S95:L5	S90:L10	S75:L25	S50:L50	S25:L75	S0:L100
$\gamma_{d,max}$ (kN/m^3) (Proctor test)		15.7	16.41	17.72	18.25	17.76	16.28	15.7
$\gamma_{d,max}$ (kN/m^3) (Vibratory table)	16.43	16.6	16.75	16.91				
$\gamma_{d,min}$ (kN/m^3) (Funnel test)	14.17	14.3	14.39	14.54				
$\gamma_{b,target}$ (kN/m^3)	16.34	16.53	16.71	18.27	19.41	19.57	18.64	18.19
$\gamma_{d,target}$ (kN/m^3)	16.3	16.47	16.61	16.84	17.33	16.87	15.47	14.91
C_c	1×10^{-5}				1.7×10^{-4}	2×10^{-4}		2.3×10^{-4}
c_L	0	0.025	0.05	0.1	0.25	0.5	0.75	1
C_r	1×10^{-5}				2.3×10^{-4}	4.1×10^{-4}		9.8×10^{-4}
c_S	1	0.975	0.95	0.9	0.75	0.5	0.25	0
C_{sw}	1×10^{-5}				2.2×10^{-5}	2.6×10^{-5}		2.9×10^{-5}
e_{max} (Funnel test)	0.829	0.813	0.802	0.785				
e_{min} (Proctor test)		0.652	0.581	0.464	0.425	0.468	0.605	0.671
e_{min} (Vibratory table)	0.578	0.562	0.549	0.535				
e_{target}	0.591	0.574	0.561	0.542	0.5	0.546	0.69	0.759
$FC_{particles}$	0	0.023	0.044	0.076	0.162	0.319	0.484	0.648
FC_{aggreg}	0				0.101	0.178	0.256	0.313
G_s	2.643	2.644	2.644	2.646	2.65	2.658	2.665	2.673
$k_{20°C}$ (m/s)	3.1×10^{-4}				1×10^{-7}	7×10^{-9}		4×10^{-9}
PI					0.01	0.04	0.07	0.11
S_a (m^2/g)	0.055	0.114	0.56	0.811	1.812	4.055	6.652	7.115
SSR	14.966	13.273	11.88	9.721	5.926	3.052	1.64	0.801
SSR^{-1}	0.067	0.075	0.084	0.103	0.169	0.328	0.61	1.248
USCS	SP	SP	SP	SP/SM	SM	SM	SM	ML
w_{hig}	2.5×10^{-3}	3.5×10^{-3}	5.8×10^{-3}	9.6×10^{-3}	1.4×10^{-2}	2.6×10^{-2}	2.9×10^{-2}	3.4×10^{-2}
w_L					0.21	0.27	0.33	0.39
w_{opt} (Proctor test)		0.015	0.045	0.085	0.12	0.16	0.205	0.22
w_P					0.2	0.23	0.26	0.28
w_{target}	0.003	0.004	0.006	0.085	0.12	0.16	0.205	0.22

ratios (SSR^{-1}, i.e. the reciprocal of SSR), is used in the current research to facilitate further correlations with soil properties.

2.2. Dimensions of particles and aggregations

Limited literature is currently available on statistical correlations between the geomechanical fill properties and the variables deemed representative of the behavior of lateritic soils. Specifically, the silica-sesquioxides ratio (SSR) is often employed for soil classification purposes as it considers soil mineralogical composition. In this context, a more extensive investigation of the statistical correlation between the geomechanical fill performance and the variables deemed as representative of these soils is discussed, based on analytical approximations developed, to better represent the experimental behavior. Specifically, the following mathematical expressions were used:

$$y = a_1 + a_2 x \tag{4}$$

$$y = b_1 e^{b_2 x} \tag{5}$$

$$y = c_1 + c_2 \ln x \tag{6}$$

where y is the dependent variable under consideration, i.e. $y = f(x)$; x represents the independent variable; e is the Euler's constant; and a_1, a_2, b_1, b_2, c_1, and c_2 are the dimensionless fitted coefficients.

A summary of the analytical approximations employed in this research is listed in Table 2, along with their respective coefficients of determination (R^2).

The specific gravity of soils (G_s) was determined according to ASTM D845-14 (2014), with results ranging from 2.64 (S100:L0) to 2.67 (S0:L100), as summarized in Table 1. A linear approximation (Eq. (4)) was adopted to represent G_s as a function of c_L, as shown in Table 2 (line i).

Conventional testing procedures were employed to determine the dimensions of individual soil particles (ASTM D422-63e2, 2007), i.e. with the use of a dispersing agent (DA) and solution stirring. Nonetheless, the double hydrometer test (ASTM D4221-18, 2018), which employs neither DA nor solution stirring, was also carried out to further evaluate the dimensions of water-stable soil aggregations. The resulting granulometric curves are shown in Fig. 2a, indicating considerable changes due to different testing procedures. It should be noted that the formation of water-stable soils aggregations was previously expected for the lateritic soil (S0:L100) (e.g. Mahalinga-Iyer and Williams, 1994; Ng et al., 2019; Araujo et al., 2021), due to the interparticle bonding capabilities of the sesquioxides. However, such behavior could also be attributed to the sand-silt mixtures containing lateritic soil (i.e. S75:L25, S50:L50, and S25:L75).

Given the potential impact of water-stable soil aggregation on the geomechanical behavior of soils, a comparison between the different granulometric curves and the sesquioxides-silica ratio (SSR^{-1}) was carried out, as presented in Fig. 2b. Specifically, cubic spline interpolation was used to provide a tridimensional perspective of the resulting granulometric surfaces, which evidenced the impact of mineralogy with increasing SSR^{-1}.

It should be noted that the fines content conventionally refers to the mass fraction associated with individual particles with a diameter smaller than 0.075 mm, following tests with the use of DA (ASTM D422-63e2, 2007). In this work, this variable is named fines content relative to individual soil particles ($FC_{particles}$). Nonetheless, this work also investigated the fines content relative to water-stable soil aggregations (FC_{aggreg}), which corresponded to the mass fraction relative to soil aggregation with diameters smaller than 0.075 mm, following tests that employed neither DA nor solution stirring. Thus, the fines content relative to individual soil particles ($FC_{particles}$) and soil aggregations (FC_{aggreg}) could be established based on the size distribution curves, as shown in Fig. 2a. Overall, based on the results, the existing gap between $FC_{particles}$ and FC_{aggreg} denoted a larger susceptibility to the

Table 2
Analytical approximations between variables obtained experimentally and fitting coefficients.

Line	$y = f(x)$	x	Equation No.	Valid domain	Fitted coefficient	R^2 (%)
i	G_s	c_L	(4)	$0 \le c_L \le 1$	$a_1 = 2.6428$, $a_2 = 0.0301$	99.9
ii	$FC_{particles}$	c_L	(4)	$0 \le c_L \le 1$	$a_1 = 0$, $a_2 = 0.647$	99.9
iii	FC_{aggreg}	c_L	(4)	$0 \le c_L \le 1$	$a_1 = 0$, $a_2 = 0.3308$	99.6
iv	SSR^{-1}	c_L	(5)	$0 \le c_L \le 1$	$b_1 = 0.0736$, $b_2 = 2.8669$	99.9
v	$FC_{particles}$	SSR^{-1}	(6)	$0.07 \le SSR^{-1} \le 1.25$	$c_1 = 0.5857$, $c_2 = 0.2218$	99.5
vi	FC_{aggreg}	SSR^{-1}	(6)	$0.07 \le SSR^{-1} \le 1.25$	$c_1 = 0.2986$, $c_2 = 0.1096$	99.6
vii	SSR^{-1}	$FC_{particles}$	(5)	$0 \le FC_{particles} \le 0.65$	$b_1 = 0.0716$, $b_2 = 4.4874$	99.9
viii	SSR^{-1}	FC_{aggreg}	(5)	$0 \le FC_{aggreg} \le 0.31$	$b_1 = 0.0659$, $b_2 = 9.0912$	98.7
ix	$FC_{particles}$	FC_{aggreg}	(4)	$0 \le FC_{aggreg} \le 0.31$	$a_1 = 0$, $a_2 = 1.944$	99.5
x	FC_{aggreg}	$FC_{particles}$	(4)	$0 \le FC_{particles} \le 0.65$	$a_1 = 0$, $a_2 = 0.512$	99.5
xi	e_{E1}	c_L	(11)	$0 \le c_L \le c_{L,opt}$	$d_1 = -0.347$	97.2
xii	e_{E2}	c_L	(12)	$c_{L,opt} \le c_L \le 1.00$	$d_2 = 0.3682$	96.3
xiii	S_a	SSR^{-1}	(6)	$0.07 \le SSR^{-1} \le 1.25$	$c_1 = 7.0411$, $c_2 = 2.6614$	97.5
xiv	S_a	$FC_{particles}$	(4)	$0 \le FC_{particles} \le 0.65$	$a_1 = 0.055$, $a_2 = 11.902$	97.9
xv	S_a	FC_{aggreg}	(4)	$0 \le FC_{aggreg} \le 0.31$	$a_1 = 0.055$, $a_2 = 23.273$	98
xvi	w_L	SSR^{-1}	(6)	$0.17 \le SSR^{-1} \le 1.25$	$c_1 = 0.3717$, $c_2 = 0.0905$	99.9
xvii	w_P	SSR^{-1}	(6)	$0.17 \le SSR^{-1} \le 1.25$	$c_1 = 0.2747$, $c_2 = 0.0406$	98.7
xviii	w_L	$FC_{particles}$	(6)	$0.16 \le FC_{particles} \le 0.65$	$c_1 = 0.4304$, $c_2 = 0.1265$	96.5
xix	w_P	$FC_{particles}$	(6)	$0.16 \le FC_{particles} \le 0.65$	$c_1 = 0.302$, $c_2 = 0.0577$	98.5
xx	w_L	FC_{aggreg}	(6)	$0.1 \le FC_{aggreg} \le 0.31$	$c_1 = 0.5491$, $c_2 = 0.1525$	95.4
xxi	w_P	FC_{aggreg}	(6)	$0.1 \le FC_{aggreg} \le 0.31$	$c_1 = 0.3566$, $c_2 = 0.0698$	98
xxii	$k_{20\,°C}$ (m/s)	SSR^{-1}	(14)	$0.07 \le SSR^{-1} \le 1.25$	$g_1 = -20.7268$, $g_2 = 0.8366$	98.7
xxiii	$k_{20\,°C}$ (m/s)	$FC_{particles}$	(14)	$0 \le FC_{particles} \le 0.65$	$g_1 = -20.3424$, $g_2 = 0,6211$	99.6
xxiv	$k_{20\,°C}$ (m/s)	FC_{aggreg}	(14)	$0 \le FC_{aggreg} \le 0.31$	$g_1 = -22.3166$, $g_2 = 0.6996$	98.4
xxv	C_c	SSR^{-1}	(15)	$0.07 \le SSR^{-1} \le 1.25$	$h_1 = 0.1031$, $h_2 = -0.0063$	99.8
xxvi	C_r	SSR^{-1}	(15)	$0.07 \le SSR^{-1} \le 1.25$	$h_1 = 0.0269$, $h_2 = -0.0015$	94.7
xxvii	C_{sw}	SSR^{-1}	(15)	$0.07 \le SSR^{-1} \le 1.25$	$h_1 = 0.01$, $h_2 = -0.0006$	98.8
xxviii	C_c	$FC_{particles}$	(16)	$0 \le FC_{particles} \le 0.65$	$i_1 = -3.45 \times 10^{-5}$, $i_2 = 0.0119$	99.9
xxix	C_r	$FC_{particles}$	(16)	$0 \le FC_{particles} \le 0.65$	$i_1 = -3.43 \times 10^{-5}$, $i_2 = 0.0009$	93.4
xxx	C_{sw}	$FC_{particles}$	(16)	$0 \le FC_{particles} \le 0.65$	$i_1 = 2.68 \times 10^{-6}$, $i_2 = 0.0001$	98.9

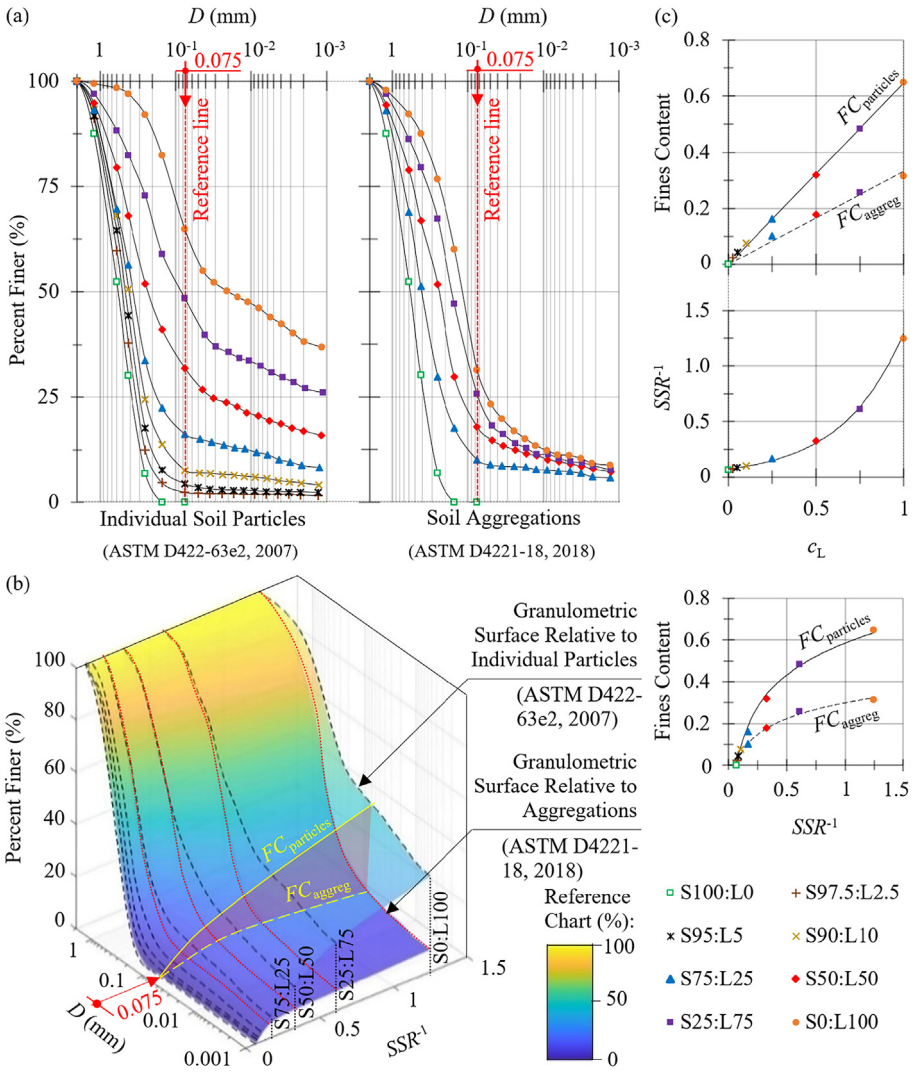

Fig. 2. Soil arrangement and sizes: (a) Granulometric curves showing particle (or aggregations) diameters, (b) Granulometric surfaces relative to individual particles and soil aggregations, and (c) Correlations between variables. Note: The variables shown are the fines content of individual soil particles ($FC_{particles}$), fines contents of soil aggregations (FC_{aggreg}), and sesquioxides-silica ratio (SSR^{-1}).

formation of water-stable soil aggregations as SSR^{-1} increased. Additionally, the formation of water-stable soil aggregations could also be attributed to the continued increase in SSR^{-1}. A comparison between variables (i.e. $FC_{particles}$, FC_{aggreg}, SSR^{-1}, and c_L) is shown in Fig. 2c, and the fitted coefficients are presented in Table 2 (lines ii-x).

Based on these results, it should be pointed out that the small increments in the lateritic soil mass fraction (c_L) are associated with the large increases in SSR^{-1}, as an exponential relationship was employed to determine SSR^{-1} as a function of c_L (as in line iv, Table 2). On the other hand, the fines content relative to the individual soil particles ($FC_{particles}$), which is conventionally employed as a design variable when addressing the effect of fine-grained soil particles on the geomechanical responses of the sand-silt mixtures, varied linearly with increases in c_L (as in line ii, Table 2). Thus, when it comes to delimiting the transitional behavior from a sand-dominant soil structure to a silt-dominant one, variable SSR^{-1} could be adequately employed to draw assumptions on the geomechanical performance of the sand-silt mixtures containing lateritic soils. This last statement is particularly valid when considering a limited share of c_L, in which the influence of the sesquioxides coating on the geomechanical behavior of the host sand is even more noticeable, due to the non-linear relationship between SSR^{-1} and c_L.

3. Aspects related to soil compaction

There is a general agreement that compaction plays an important role in the geomechanical performance of lateritic soils (e.g. Al Haj and Standing, 2016; Silva et al., 2021) since the plastic, textural, and overall engineering characteristics of these soils can be largely impacted by soil remolding (Townsend et al., 1971).

A series of laboratory tests was performed to investigate the performance of the compacted sand-silt mixtures containing lateritic soil. Standard Proctor compaction tests (ASTM D698-12, 2021) were carried out considering the mixtures (i.e. S97.5:L2.5, S95:L5, S90:L10, S75:L25, S50:L50, and S25:L75) and lateritic soil (S0:L100). The testing results are summarized in Tables 1 and i.e. maximum dry unit weights ($\gamma_{d,max}$) and optimum water contents (w_{opt}), and a representation of these parameters is shown in Fig. 3a concerning SSR^{-1}, $FC_{particles}$, and FC_{aggreg}.

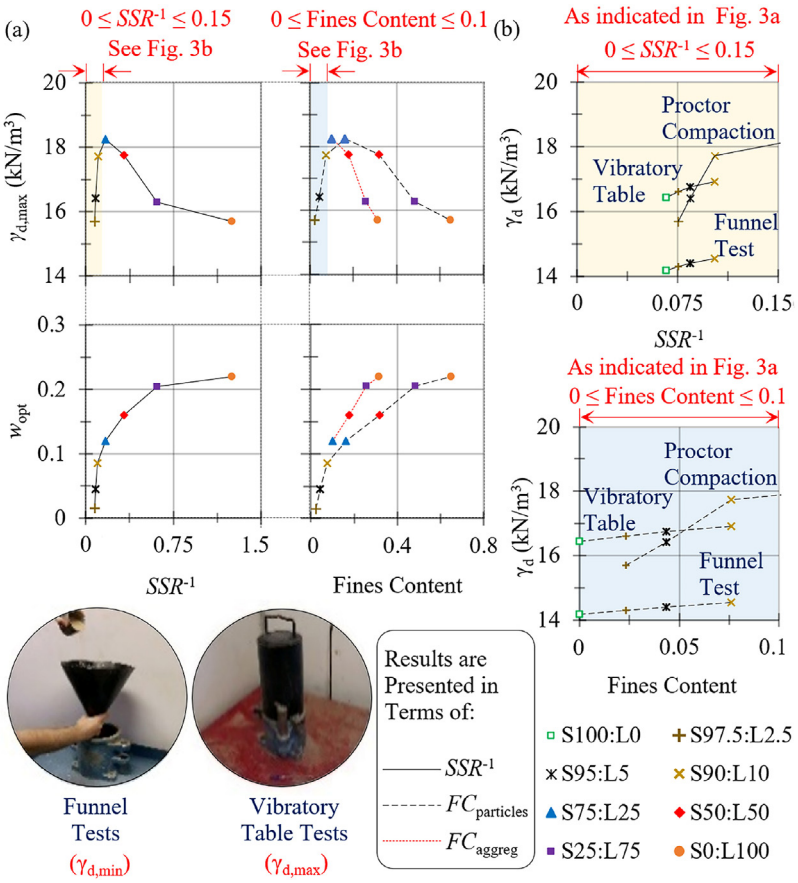

Fig. 3. Soil compaction properties: (a) Standard effort proctor compaction, i.e. maximum dry unit weights ($\gamma_{d,max}$) and optimum water contents (w_{opt}); and (b) Soil dry unit weights (γ_d) associated with maximum and minimum compaction ($\gamma_{d,max}$ and $\gamma_{d,min}$, respectively).

Based on the results, as the share of lateritic soil contained in the mixtures increases, which is also translated into an increase in the sesquioxides content relative to silica (SSR^{-1}) and the additional fines contents ($FC_{particles}$ and FC_{aggreg}), additional water is required to achieve proper compaction. Nonetheless, a clear maximum value of dry unit weight could be attributed to the mixture S75:L25.

The host sand (S100:L0) and mixtures S97.5:L2.5, S95:L5, and S90:L10 were subjected to vibratory table tests (ASTM D4253-16e1, 2016) and funnel tests (ASTM D4254-16, 2016) to investigate the range of mixtures that could reach a more considerable range of compaction under vibration rather than with mechanical compaction. Samples containing hygroscopic water contents (w_{hig}) were subjected to vibratory table tests and funnel tests. Accordingly, the test results are summarized in Table 1, and a comparison between the maximum dry unit weights obtained through standard Proctor tests and vibratory table tests is shown in Fig. 3b, along with the minimum dry unit weights associated with funnel tests. Based on the results, vibratory table tests were the most adequate test procedure to achieve greater compaction of samples S100:L0, S97.5:L2.5, and S95:L5 (group 1, i.e. sandy soils), while standard Proctor compaction tests could lead to greater compaction for S90:L10, S75:L25, S50:L50, S25:L75, and S0:L100 (group 2, i.e. silty soils).

The target values of unit weights (γ), i.e. bulk ($\gamma_{b,target}$) and dry ($\gamma_{d,target}$) unit weights, were established, along with the corresponding water contents (w_{target}). It should be noted that the relative densities associated with group 1 refer to the vibratory table and funnel tests, while relative compactions of group 2 consider standard Proctor test results, leading to the following compaction requirements (Berg et al., 2009): (1) a relative density of 95% for soils belonging to group 1, with a tolerance of ±3% $\gamma_{d,target}$; and (2) relative compaction of 95%, with tolerances of ±3% $\gamma_{d,target}$ and ±2%w_{target}, for soils belonging to group 2. Adopted values are summarized in Table 1, and an illustration of compaction variables relative to different domains is shown in Fig. 4, denoting a major influence of the lateritic soil on the results.

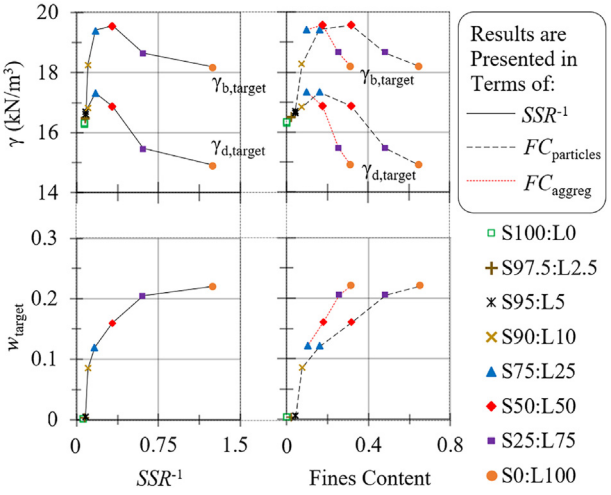

Fig. 4. Adopted soil compaction properties, i.e. soil unit weight (γ) relative to bulk ($\gamma_{b,target}$) and dry ($\gamma_{d,target}$) conditions, and water content (w_{target}).

3.1. Optimum soil packing

Fine-grained soil particles often exhibit a considerably distinct geomechanical behavior relative to the coarse-grain soil skeleton (e.g. Xenaki and Athanasopoulos, 2003; Yin et al., 2014; 2016; Yang et al., 2006), which could lead to relevant technical implications when employing the sand-silt mixtures as structural fills. In this context, engineers have investigated means to categorize the sand-silt mixtures into broader soil categories, which could share similarities in their geotechnical performance.

This research employs the concept of a dominant particle network (e.g. Chang and Yin, 2011; Chang et al., 2015), based on which the sand-silt mixtures could be categorized into one of the following soil groups: (1) sand-dominant soils, which are largely impacted by the coarse-grain soil skeleton; and (2) silt-dominant soils, which could relate to a more significant influence of fine-grained soil particles. Soil compaction tests served as a reference for delimiting these major soils groups, i.e. by providing insight into the relationship between soil void ratios (e) and lateritic soil mass fraction (c_L), as shown in Fig. 5a, with the void ratios (e) associated with target compaction requirements (Table 1).

It should be noted that, as shown in Fig. 5a, limiting boundaries could be attributed to the feasible mixture proportions (Chang et al., 2015), i.e. one upper limit boundary (B1) and two lower limit boundaries B2 and B3. Also, lower boundary B2 may assume negative values for void ratios as it considers the theoretical development proposed by Chang et al. (2015), even though it represents an unfeasible set of mixture contents.

Based on the results shown in Fig. 5a and considering the concepts presented by Chang et al. (2015), the following equations are proposed to represent the experimental results in the current research:

$$e_{B1} = e_S + (e_L - e_S)c_L \tag{7}$$

$$e_{B2} = e_S + (-1 - e_S)c_L \tag{8}$$

$$e_{B3} = e_L c_L \tag{9}$$

where e_{B1}, e_{B2} and e_{B3} stand for the void ratios associated with the theoretical limit boundaries B1, B2 and B3, respectively; and e_S and e_L denote the void ratios of the host sand and lateritic soil, respectively.

As shown in Chang et al. (2015), the intersection between lines B2 and B3 determines the transition from a sand-dominant range to a silt-dominant range. Specifically, considering model variables used in this research (Fig. 5a), the sand-dominant range would have the c_L in the range of $0 \leq c_L \leq c_{L,opt}$, while the silt-dominant range

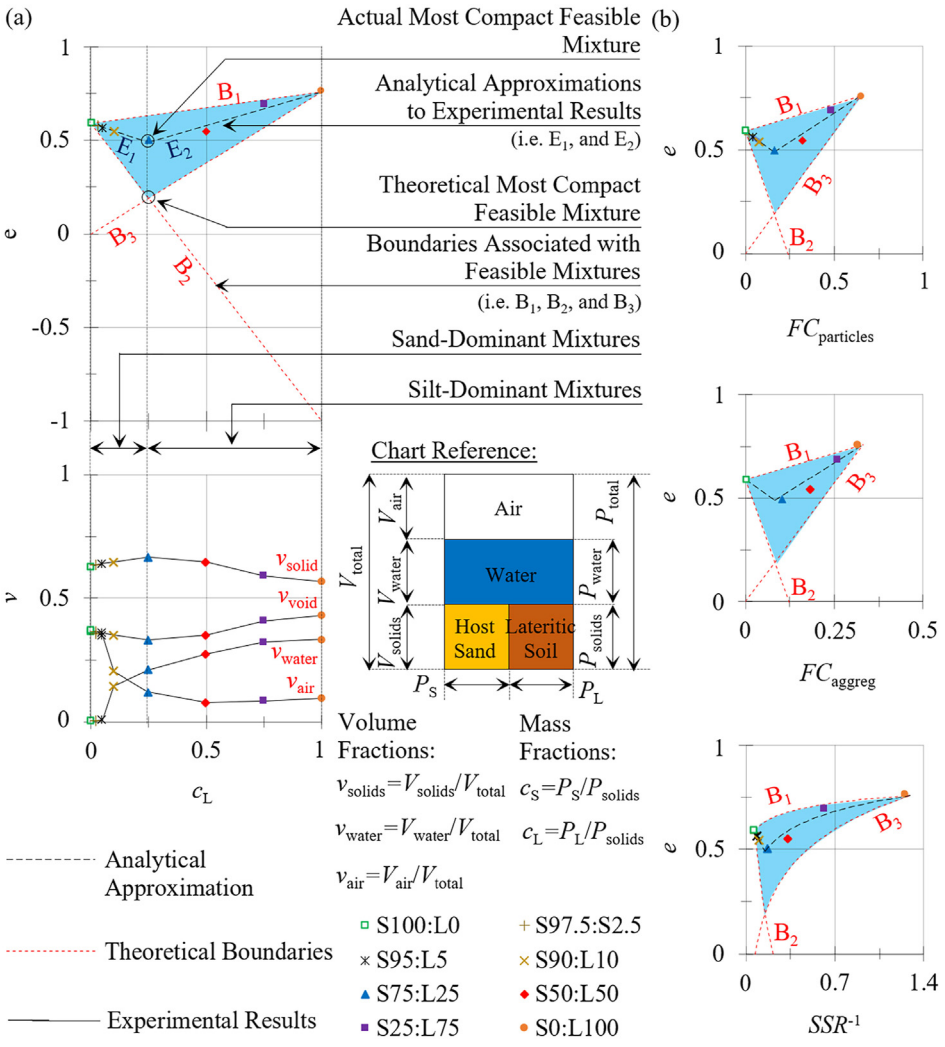

Fig. 5. Internal soil structure: (a) Representation of void ratios and volume fractions in terms of c_L; and (b) Representation of void ratios relative to fines contents and SSR^{-1}.

would refer to $c_{L,opt} < c_L \leq 1$, with $c_{L,opt}$ being the optimum lateritic soil mass ratio, i.e. the lateritic soil mass ratio that could lead to an optimum soil packing. By assuming that e_{B2} (as in Eq. (8)) matches e_{B3} (as in Eq. (9)) at the data point corresponding to the optimum lateritic soil mass ratio ($c_{L,opt}$), the following equation may be established:

$$c_{L,opt} = \frac{e_S}{1 + e_S + e_L} \tag{10}$$

where e_S and e_L refer to the void ratios of the host sand and lateritic soil, respectively.

The test results must, by definition, fall within the area delimited by the boundaries B1, B2 and B3. Therefore, based on these assumptions, a linear analytical approximation was employed to further represent test results in Fig. 5a, with E1 representing the sand-dominant range, and E2 denoting the silt-dominant range. The following equations were used in this regard:

$$e_{E1} = e_S + d_1 c_L \tag{11}$$

$$e_{E2} = e_L + d_2 (c_L - 1) \tag{12}$$

where e_{E1} and e_{E2} stand for the void ratios associated with experimental results considering lines E1 and E2, respectively; and d_1 and d_2 are the fitted coefficients (see Table 2).

Based on Eqs. (11) and (12), the parameters d_1 and d_2 were equal to −0.3470 and 0.3682, respectively, and are also summarized in Table 2 (lines xi-xii). It should be emphasized that d_1 and d_2 are dependent on the adopted compaction requirements (Chang et al., 2015), i.e. type of testing, relative density, and relative compaction. Nonetheless, it should also be observed that E1 intercepts E2 at the optimum void ratio, calculated as

$$e_{opt} = \frac{d_1 d_2 + e_S d_2 - e_L d_1}{d_2 - d_1} \tag{13}$$

where $c_{L,opt}$ stands for the optimum lateritic soil mass ratio, and e_{opt} is the correlated optimum void ratio.

Fig. 5a shows a soil phases diagram, denoting the most relevant mass and volume fractions, i.e. the volume fractions (v) of solids (v_{solids}), water (w_{water}), and air (v_{air}). A comparison of these variables concerning the lateritic soil mass ratios (c_L) is also represented in Fig. 5a. Based on these results, it becomes more evident that mixture S75:L25 relates to a denser soil packing in comparison with other sand-silt mixtures, which is consistent with the analytical evaluation based on the dominant particle network.

The void ratios (e) are presented in terms of the variables $FC_{particles}$, FC_{aggreg} and SSR^{-1} in Fig. 5b. When considering e as the independent variable and $FC_{particles}$ and FC_{aggreg} as the domains of the function $y = f(x)$, the resulting chart relates to that shown in Fig. 5a, despite differences in the magnitude of considered variables. On the other hand, when the domain of the function referred to SSR^{-1}, it may be observed that the mineralogy plays an important role in soil packing attributes, i.e. slight differences in SSR^{-1} could lead to considerable changes in particle arrangement, thereby supporting further evaluation on such behavior.

To further investigate the variables related to soil packing, a schematic representation of the soil phases is presented in Fig. 6. Accordingly, the voids of the host sand (S100:L0) are progressively filled as the lateritic soil fraction (c_L) increases, up to its optimum mass ratio ($c_{L,opt}$, i.e. mixture S75:L25), which is associated with the sand-silt mixture containing the greatest volume fraction of solids (v_{solids}). It should also be noted that the minimum volume fraction of air (v_{air}) corresponded to the mixture S50:L50, which also

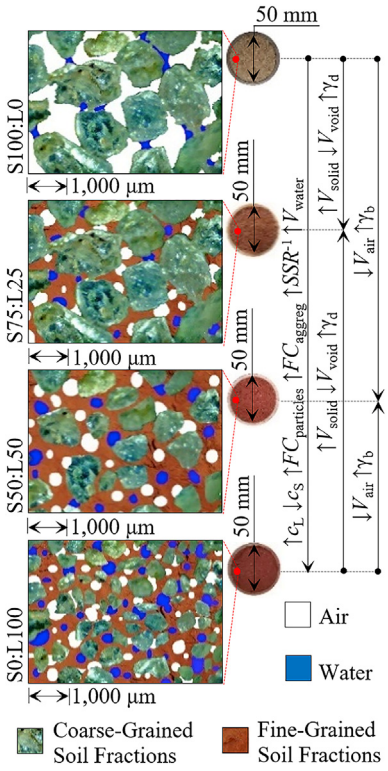

Fig. 6. Schematic representation of soil internal structure of the sand-silt mixtures containing lateritic soil.

demanded a larger amount of water to reach adequate compaction, resulting in an overall less dense soil structure relative to mixture S75:L25.

3.2. Particle arrangement

Optical microscopy tests were employed to enable the visualization of the soil particles and major soil aggregations, i.e. providing insight into macroscopic soil attributes, as shown in Fig. 7a. When considering the host sand (S100:L0), quartz, muscovite, kaolinite and rutile crystals could be visualized, which agrees with mineral composition test results as previously shown in Fig. 1b. Accordingly, when considering after-compaction disturbed samples obtained from the lateritic soil (S0:L100), major crystals corresponding to quartz, anatase, and rutile crystals could be identified and remained bounded due to the influence of the sesquioxide coating as previously shown in Fig. 1c. Fine-grained soil fractions (i.e. gibbsite, hematite and kaolinite) could not be further distinguished under optical microscopy tests, even though the interparticle-bounding was evident.

Scanning electron microscopy (SEM) analyses were performed to provide an additional understanding of the microstructure of the sand-silt mixtures containing lateritic soil, i.e. soil aggregations obtained from the compacted samples were subject to testing. FEI Quanta 450 microscope containing energy-dispersive X-ray spectroscopy (EDS) detector was used in this regard. This last device (EDS coupling) enabled qualitative measurements of chemical composition at pre-defined positions, i.e. P1, P2, P3 and P4, which are represented in Fig. 7b along with test results. Overall, based on the results, the following observations were drawn: (1) major mineral crystals, such as quartz (P1) and anatase or rutile (P3) could be identified; while (2) sesquioxides-coating, attributed to

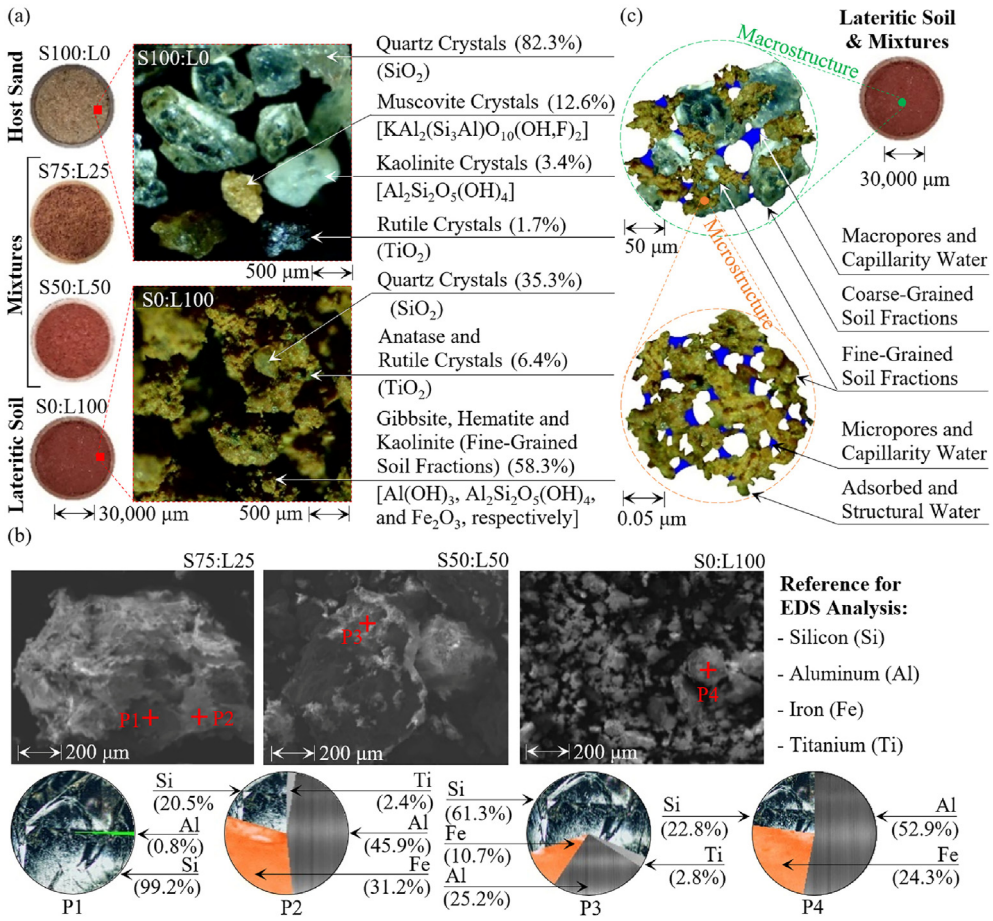

Fig. 7. Arrangement of soil particles: (a) Optical microscopy visualization of host sand (S100:L0) and lateritic soil (S0:L100), (b) Schematic representation of macro- and microstructure relative to selected samples containing lateritic soil, and (c) SEM and EDS test results considering selected samples containing lateritic soil.

positions P2 and P4, could provide an interparticle-bonding to major soil particles.

A schematic representation of particle arrangement is indicated in Fig. 7c, which is deemed representative of the sand-silt mixtures and lateritic soil. From the macrostructure perspective, coarse-grained soil fractions remained bounded by fine-grained soil fractions, and the corresponding macropores could entail relevant shares of capillarity water and air. Accordingly, from the microstructural point of view, fine-grained soil fractions could be associated with the formation of micropores, which could either be filled with air or water. This bimodal pore size, which is characteristic of intensely weathered tropical soils, could also have a significant impact on the overall geomechanical performance of the sand-silt mixtures.

4. Geomechanical behavior

A summary of the geomechanical characteristics discussed in this section is also presented in Table 1, and a representation of these testing results is shown in Fig. 8. The following mathematical expressions were also employed to better represent experimental behavior, which is further discussed in this section of the paper:

$$y = e^{g_1 + \frac{g_2}{x}} \tag{14}$$

$$y = h_1 + \frac{h_2}{x} \tag{15}$$

$$y = \sqrt{i_1 + i_2\sqrt{x}} \tag{16}$$

where g_1, g_2 h_1, h_2, i_1 and i_2 are the fitted coefficients.

4.1. Physical and geotechnical properties

The specific surface area (S_a) of individual soil particles was evaluated using a Nova 2200e apparatus (Quantachrome Instruments), given the potential influence of this feature on the geomechanical behavior of fine-grained soils (Mitchell and Soga, 2005). Sample preparation and testing procedures followed the specifications described in Arnepalli et al. (2008), with Nitrogen (N_2) being employed as an adsorbate during testing. The Brunauer-Emmett-Teller (BET) theory (Brunauer et al., 1938) supported these analyses. A schematic representation of the results is shown in Fig. 8a in terms of sesquioxide-silica ratios (SSR^{-1}), and fines contents, i.e. individual soil particles ($FC_{particles}$) and soil aggregations (FC_{aggreg}) with a diameter smaller than 0.075 mm. As it concerns the SSR^{-1} domain, a logarithmic relationship (Eq. (6)) was deemed suitable to represent the experimental behavior (Table 2, line xii), while a linear correspondence (Eq. (4)) could better describe S_a with respect to $FC_{particles}$ and FC_{aggreg} (Table 2, lines xiv-xv).

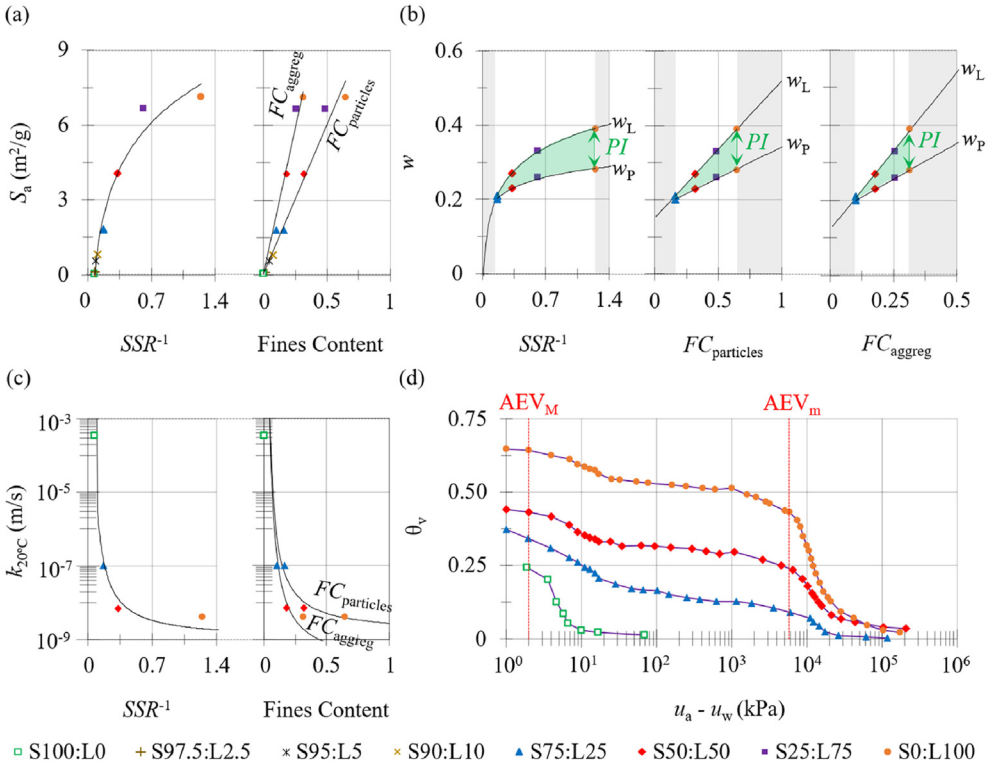

Fig. 8. Soil properties and correlated variables: (a) Soil surface area, (b) Atterberg limits, (c) Saturated hydraulic conductivity, and (d) Water retention curves.

Atterberg limits (ASTM D4318-17e1, 2017) were also determined. A summary of testing results is presented in Table 1, while a schematic representation of findings associated with this behavior (i.e. plastic limits (w_P), liquid limits (w_L), and their corresponding ranges of plasticity indices (PI)) is shown in Fig. 8b, in terms of SSR^{-1}, $FC_{particles}$ and FC_{aggreg}. A logarithmic approximation (Eq. (6)) was implemented to represent w_P and w_L in the SSR^{-1} domain, while a linear approximation (Eq. (4)) could be used in this regard when considering the $FC_{particles}$, and FC_{aggreg} domains. A summary of fitted coefficients is presented in Table 2 (lines xvi-xxi). Based on these results, the plastic behavior presented by sample S75:L25 (with PI of about 1%) could denote a transition from a coarse-grained soil skeleton dominance to a fine-grained one.

Based on the soil properties such as the particle size distribution, the specific gravity of solids, and Atterberg limits, it was possible to employ the unified soil classification system (USCS) (ASTM D4287-17e1, 2017) to cluster the sand-silt mixtures into different soil categories, as the results summarized in Table 1. Specifically, samples S100:L0, S97.5:L2.5 and S95:L5 were classified as poorly graded sands (SP), while sample S90:L10 could be better represented by the poorly graded sand with silt group (SP/SM). Samples S75:L25, S50:L50 and S25:L75 were categorized as silty sands (SM), and the lateritic soil (S0:L100) fell into the lean silt (ML) soil group.

Constant head (ASTM D2434-19, 2019) and falling head (ASTM D5084-16a, 2016) hydraulic conductivities were also evaluated. Specifically, the host sand (S100:L0) was subjected to constant head tests, while samples S75:L25, S50:L50 and S0:L100 were subjected to falling head tests. Results are summarized in Table 1A representation of the hydraulic conductivity at 20 °C ($k_{20\,°C}$) in terms of SSR^{-1} and fines contents (i.e. $FC_{particles}$ and FC_{aggreg}) is shown in Fig. 8c. The analytical expression indicated in Eq. (14) was found suitable to represent the relationship between these variables, with fitted coefficients indicated in Table 2 (lines xxii-xxiv). Overall, minor changes in both SSR^{-1}, $FC_{particles}$, and FC_{aggreg}, could lead to a considerable decrease in hydraulic conductivity. Based on the observed behavior, the hydraulic conductivity of the host sand (S100:L0) could relate to free-draining sand, while other samples better associated with clayey soils, as in the classification proposed by Shackelford (2013).

When considering geosynthetic-reinforced soil walls, it should be noted that matric suction may have a significant impact on the loads transmitted through the system (Portelinha et al., 2021). Nonetheless, previous authors have also identified matric suction as a relevant factor of influence on the internal shear strength and compressibility of lateritic soils (e.g. Riccio et al., 2014), which could be attributed to the water-retention capabilities of the porous micro-aggregations found in these materials (Townsend et al., 1971). On top of these considerations, the sand-silt mixtures containing lateritic soil could lack adequate drainage capabilities, which could potentially lead to structural problems caused by rainwater infiltration (e.g. Xiao et al., 2021).

In this context, the soil-water retention curves (SWRCs) were determined to further investigate the potential implications of employing the sand-silt mixtures as structural fills in reinforced soil walls. A series of laboratory tests was performed to provide insight into the volumetric water contents (θ_v) and their corresponding matric suctions ($u_a - u_w$), where u_a refers to air pressure and u_w denotes water pressure. Specifically, the following test methods were employed: (1) pressure plate apparatus, considering $u_a - u_w$ in the range of 1 kPa–17 kPa; (2) filter paper tests (ASTM D5298-16, 2016), considering $u_a - u_w$ in the range of 17 kPa–100 kPa; and (3) dewpoint meter equipment (WP4C, manufactured by Decagon Devices) for levels above 100 kPa of $u_a - u_w$.

The various SWRCs are shown in Fig. 8d, with an indication of the air entry values (AEV) associated with macropores (AEV_M) and micropores (AEV_m). Specifically, average values of 4 kPa and 7500 kPa could be attributed to AEV_M and AEV_m, respectively, based

on the experimental results. The following relation was employed to provide estimates of pore diameters (e.g. Zhang and Li, 2010):

$$u_a - u_w = \frac{4\sigma_w \cos\theta_w}{D_p} \quad (17)$$

where $u_a - u_w$ is the matric suction, σ_w refers to the surface tension of water (0.0728 N/m), θ_w is the water-solid contact angle (assumed as 0°), and D_p is the pore diameter.

Considering Eq. (17), an average dimension of 70 μm could be attributed to macropores, while an average dimension of 0.04 μm could be related to micropores. It should be noted that this bimodal soil structure, in which a transition from a macrostructure domain to a microstructure domain occurs, was characteristic of the sand-silt mixtures containing lateritic soil (S75:L25, S50:L50 and S0:L100), while the host sand (S100:L0) was primarily governed by macropores (unimodal soil structure). These results corroborate the assumptions drawn in Fig. 7c, further evidencing the impact of particle arrangement on the geomechanical behavior of these marginal fills.

One-dimensional (1D) consolidation tests (ASTM D2435/D2435M-11, 2020) were performed under the inundated testing conditions. Specifically, the compacted soil specimens satisfied the compaction requirements indicated in Table 1, with tolerances of $\pm 3\%\gamma_{d,target}$ and $\pm 2\%w_{target}$ for the dry unit weights and compaction water contents, respectively. Effective vertical stresses (σ'_v) ranging from 5 kPa to 400 kPa were employed during the loading and unloading stages. The void ratios (e) obtained after each loading stage are represented in terms of σ'_v in Fig. 9a, along with the corresponding coefficients (Fig. 9b), i.e. compression indices (C_c), recompression indices (C_r), and swelling indices (C_{sw}). A summary of the testing results is also presented in Table 1. Based on these results, the analytical relation indicated in Eq. (15) was found suitable to represent C_c, C_r and C_{sw} in terms of SSR^{-1} (Table 2, lines xxv-xxvi), while Eq. (16) could be employed to represent C_c, C_r and C_{sw} in terms of $FC_{particles}$ (Table 2, lines xxviii-xxx).

Overall, based on the results discussed in this section, the following aspects should be emphasized: (1) the variable SSR^{-1}, which is inherently associated with the mineral composition of the sand-silt mixtures containing lateritic soil, could provide a reliable tool to predict the geomechanical responses, while also facilitating the delimitation of major coarse-grained and fine-grained ranges of influence; and (2) the fines contents, i.e. individual soil particles ($FC_{particles}$) and soil aggregations (FC_{aggreg}) with a diameter smaller than 0.075 mm, can further improve the predictive capabilities of the studied methods for geotechnical behavior.

4.2. Soils internal shear resistance

Direct shear tests (ASTM D3080/D3080M-11, 2011) were performed to provide insight into internal friction angles and cohesive intercepts of compacted soils, and the testing results are shown in Fig. 10. In this research, the following analytical expression was employed to represent friction angles in terms of initial vertical stresses in Fig. 10 (Pierozan et al., 2022):

$$y = e^{j_1 + j_2 \ln\left(\frac{\sigma_{v,0}}{p_a}\right)} \quad (18)$$

where $\sigma_{v,0}$ represents the initial vertical stresses; j_1 and j_2 are the fitted coefficients, as summarized in Table 3; and p_a is the atmospheric pressure (= 101 kPa).

Specifically, tested specimens met compaction requirements indicated in Table 1, with tolerances of $\pm 3\%\gamma_{d,target}$ and $\pm 2\%w_{target}$ for dry unit weights and compaction water contents, respectively. Consolidation and shear stages were conducted with the use of specimens subjected to the following testing conditions: (1) inundated, with after-test degrees of saturation ranging from 85% to 90%; and (2) non-inundated, with water contents remaining in the range of $\pm 2\%w_{target}$ both before and after testing. A constant shear displacement rate of 0.05 mm/min was adopted to avoid excess pore pressure.

In light of the tests conducted under the inundated conditions, a representation of internal shear resistance parameters is shown in Fig. 10a. Specifically, the shear stresses (τ) and vertical shear displacements (δ_v) are plotted in terms of the horizontal shear displacements (δ_h), while the maximum shear stresses (τ_{max}) and the corresponding secant internal soil friction angles ($\phi_{i,sec}$) are represented in terms of initial vertical stresses ($\sigma_{v,0}$), with subscript "i" indicating tests conducted under the inundated conditions. Accordingly, soil internal friction angles of 43°, 39°, 37° and 32°, and the cohesive intercepts of 0 kPa, 5 kPa, 9 kPa and 10 kPa could be attributed to soils S100:L0, S75:L25, S50:L50 and S0:L100, based on their respective Mohr-Coulomb envelopes. Soil secant friction angles ($\phi_{i,sec}$) were determined based on the test results, with the analytical expression denoted by Eq. (18) being employed to gain insight into the relationship between $\phi_{i,sec}$, and $\sigma_{v,0}$. A summary of fitted coefficients (j_1 and j_2) is shown in Table 3.

A detailed description of results associated with non-inundated specimens can be found in Pierozan et al. (2022), according to which soil internal friction angles of 44°, 40°, 38° and 33°, and the cohesive intercepts of 0 kPa, 11 kPa, 21 kPa and 30 kPa could be attributed to soils S100:L0, S75:L25, S50:L50 and S0:L100, based on

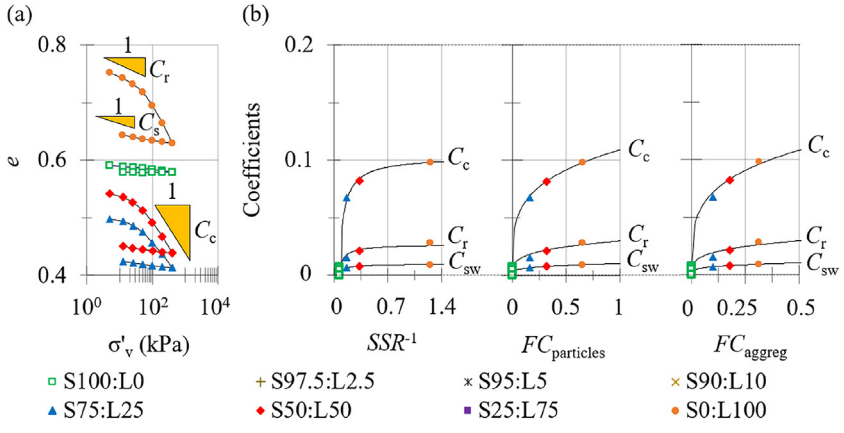

Fig. 9. 1D consolidation tests results: (a) Loading and unloading consolidation curves, and (b) Consolidation coefficients.

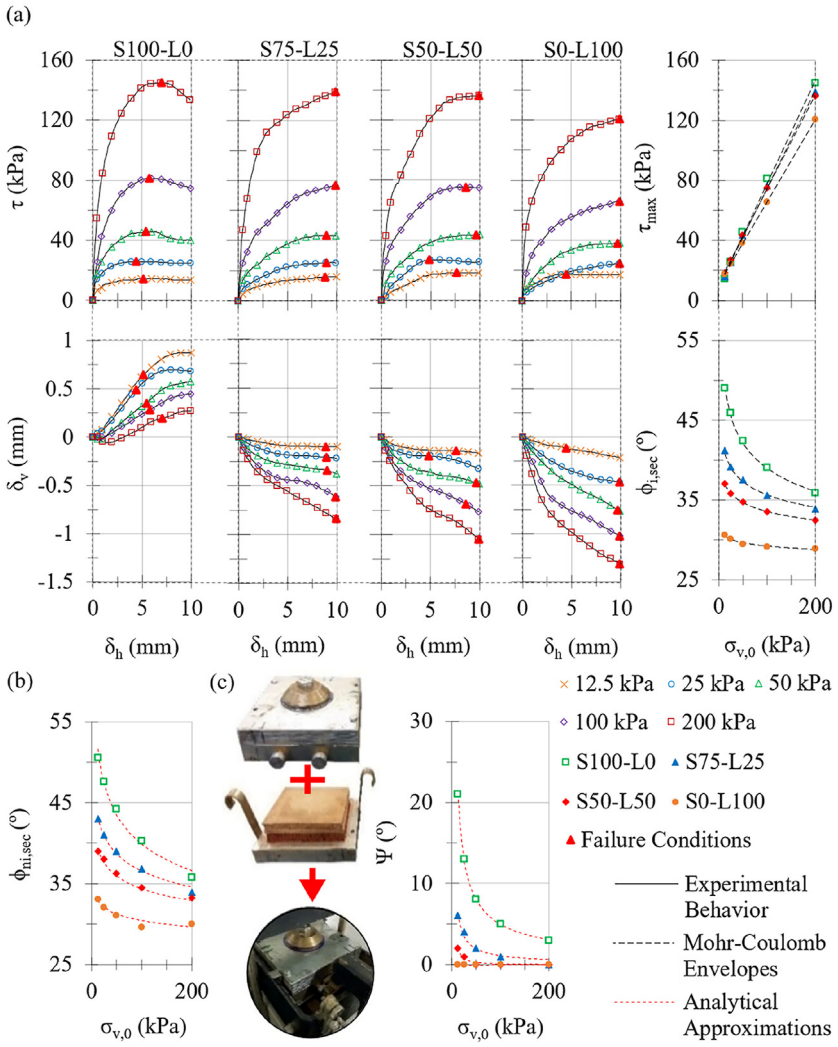

Fig. 10. Direct shear test results: (a) Internal shear resistance relative to inundated tests, (b) Comparison of internal shear resistance relative to inundated and non-inundated tests, and (c) Dilation angles relative to non-inundated tests.

their respective Mohr-Coulomb envelopes. The corresponding secant internal soil friction angles ($ø_{ni,sec}$) are shown in Fig. 10b in terms of initial vertical stresses ($\sigma_{v,0}$). The subscript "ni" indicates tests conducted in non-inundated (unsaturated) conditions. Experimental results were also subjected to an analytical approach (Eq. (18)), with the corresponding coefficients j_1 and j_2 summarized in Table 3. Based on these results, the cohesive intercepts associated with inundated tests had a considerably lower magnitude relative to non-inundated tests (unsaturated), further denoting the influence of matric suction on internal shear resistance (as in Fig. 8d). Conversely, the soil internal friction angles were not subjected to substantial changes when comparing inundated and non-inundated tests.

An alternative testing procedure was employed to evaluate the dilation angles relative to the direct shear tests (e.g. Jewell, 1989; Simoni and Houlsby, 2006), given that plane strain and axisymmetric testing conditions may lead to similar angles of dilation (Schanz and Vermeer, 1996). In this context, the upper frame of the direct shear apparatus was attached to the piston at which the normal load are applied, thus providing a uniform distribution of vertical displacements on top of the tested soil specimens, as shown in Fig. 10c. A detailed description of these tests is presented in Pierozan et al. (2022), and an indication of testing results and analytical approximation (Eq. (18)) is also presented in Fig. 10c, with the corresponding coefficients j_1 and j_2 summarized in Table 3. Overall, by comparing the different testing procedures discussed in this paper, a dilatant behavior could be attributed to the samples containing larger shares of coarse-grained soil particles, which also impacted the corresponding soil internal friction angles.

5. Application as structural fills

The internal stability of reinforced soil structures relies on the interfacial resistance mechanisms that develop between the structural fill soil and the linear reinforcement inclusions within this material (e.g. Schlosser and Bastick, 1991), i.e. soil-reinforcement interface shear and bearing resistances. Theoretical, numerical and experimental methods have been widely employed to study and understand such resistance mechanisms that develop under the field conditions, such as reinforcement pullout in the anchorage zone. The use of polymeric strips may be particularly advantageous when dealing with the sand-silt mixtures containing lateritic soil, given the corrosive potential of metallic strips installed within humid environments.

A schematic representation of a reinforced soil structure using polymeric strips is shown in Fig. 11a, with an indication of how such

Table 3
Analytical approximations between direct shear test results and vertical stresses.

Testing condition	$y = f(\sigma_{v,0})$	Equation No.	Valid domain	Tested soil	Fitted coefficient	R^2 (%)
Inundated	$\phi_{i,sec}$ (°)	(18)	12.5 kPa ≤ $\sigma_{v,0}$ ≤ 200 kPa	S100:L0	$j_1 = 3.662$, $j_2 = -0.1124$	99.8
				S75:L25	$j_1 = 3.573$, $j_2 = -0.0657$	99.2
				S50:L50	$j_1 = 3.513$, $j_2 = -0.0471$	99.9
				S0:L100	$j_1 = 3.375$, $j_2 = -0.0209$	97.6
Non-Inundated	$\phi_{ni,sec}$ (°)	(18)		S100:L0	$j_1 = 3.685$, $j_2 = -0.1243$	99
				S75:L25	$j_1 = 3.598$, $j_2 = -0.0813$	98.6
				S50:L50	$j_1 = 3.536$, $j_2 = -0.0641$	98.4
				S0:L100	$j_1 = 3.414$, $j_2 = -0.0372$	94.7
	Ψ (°)	(18)		S100:L0	$j_1 = 1.593$, $j_2 = -0.695$	99.9
				S75:L25	$j_1 = 0.0939$, $j_2 = -0.8293$	97
				S50:L50	$j_1 = -2.284$, $j_2 = -1.436$	95.5
				S0:L100	$j_1 = -4.605$, $j_2 = 0.0003$	99.9
	$\sigma_{v,max}$ (kPa)	(21)	12.5 kPa ≤ $\sigma_{v,0}$ ≤ 50 kPa	S100:L0	$f^*/f = 2.0747$	99.7
				S75:L25	$f^*/f = 1.5051$	99
				S50:L50	$f^*/f = 1.2808$	99.1
				S0:L100	$f^*/f = 1.1699$	99.9
	P_{max} (kN)	(23)		S100:L0	$k_1 = -0.8019$, $k_2 = 7.434$	98.9
				S75:L25	$k_1 = 0.0427$, $k_2 = 4.34$	99.7
				S50:L50	$k_1 = 0.1666$, $k_2 = 3.106$	98.7
				S0:L100	$k_1 = 0.2$, $k_2 = 2.071$	99.9

Note: Specimens used for direct shear tests met the following compaction criteria: initial water content of approximately 0.25%, and relative density of 95% ± 3%, for sample S100-L0; and initial water content of w_{target} ± 2%, and relative compaction of 95% ± 3%, for samples S75-L25, S50-L50 and S0-L100. In light of non-inundated tests, water contents remained in the range of ±2%w_{target} before and after testing.

conditions could be simulated in a laboratory-controlled environment (e.g. Palmeira, 2004, 2009). Specifically, the apparatus as shown in Fig. 11a was employed in the current research to gain insight into reinforcement pullout resistances. A vertical cross-section of the pullout testing equipment used in the experimental component of this study is presented in Fig. 11b, with an overview of the most relevant components of the device given in Fig. 11c.

The pullout box was originally designed by Palmeira (1996), and subsequently enhanced by Pierozan (2018) with a series of components, including a flexible hydraulic diaphragm-loading device, horizontal and vertical reaction frames, enhanced geosynthetic clamps, pullout actuator, and instrumentation. The double strap arrangement (e.g. Miyata et al., 2019) was employed in this research. In this reinforcement configuration, the polymeric strips were installed in closely spaced pairs oriented perpendicular to the facing unit (Fig. 11b and c).

The width of a single polymeric strip reinforcement was 50 mm, which is denoted as b_s in Fig. 11b. Accordingly, the distances between the external and internal boundaries of the strips are represented by b_e and b_i, respectively, leading to a total reinforcement width (W_g) of 100 mm. The reported tensile strength of each polymeric strip was 50 kN, taking advantage of a high tenacity polyester fiber (HTPET) reinforced core protected by a polyethylene sheet encasement. The elastic moduli of each polymeric strip were equal to 2.43 GPa and 2.27 GPa at 2% and 5% strain levels, respectively.

A horizontal cross-section on the reinforcement installation level is represented in Fig. 11c, indicating the following instrumentation devices: one load cell and two displacement transducers. A computer-controlled data acquisition system was connected to the instrumentation devices. A series of pressure cells was also implemented into the pullout box to provide insight into stress distribution during testing, which is further detailed in Pierozan et al. (2022). The internal surfaces of the pullout box were covered with double layers of lubricant and polyethylene film to reduce sidewall friction.

Pullout tests were conducted in non-inundated conditions. For sample S100-L0, the initial water content was set to approximately 0.25% and the relative density was 95% ± 3%. For samples S75-L25, S50-L50, and S0-L100, the initial water content was set to ±2% w_{target} and the relative compaction was 95% ± 3%. Sand pluviation and vibration techniques were employed to achieve the target density for sample S100:L0, while compaction using a mechanical hammer was performed on samples S75:L25, S50:L50 and S0:L100. Initial vertical stresses ($\sigma_{v,0}$) of 12.5 kPa, 25 kPa and 50 kPa were adopted for testing, considering the reinforcement level. The rate of displacement was 1 mm/min, and the maximum displacement of the external end of the strips was 100 mm. ASTM D6706-01 (2013) served as a reference for the pullout tests.

5.1. Conceptualization

The initial vertical stress ($\sigma_{v,0}$) acting on the reinforcement plane during pullout encompasses the surcharge stress, which is applied by loading devices on the upper surface of the compacted soil, and the vertical geostatic soil pressure on the reinforcement, which depends on the confinement level attributed to the compacted soil. Nonetheless, it should be noted that a local increase in vertical stresses may develop on the soil-reinforcement interface during pullout tests when dealing with compact and dilatant fills, such as clean sands and gravels (e.g. Kido and Kimura, 2021). Specifically, under failure conditions (peak shear stresses), the following equation accounts for the real stresses acting on the reinforcement level:

$$\sigma_{v,max} = \sigma_{v,0} + \Delta\sigma_{v,max} \tag{19}$$

where $\sigma_{v,max}$ is the actual vertical stress acting on reinforcement level under failure conditions, $\sigma_{v,0}$ is the initial vertical stress, and $\Delta\sigma_{v,max}$ refers to the local increase in vertical stress under failure conditions.

Currently, available design procedures for geosynthetic reinforced earth walls often rely on estimates concerning friction coefficients based on soil geomechanical characteristics. Given the different theoretical assumptions relative to vertical stresses acting on reinforcement level, the maximum shear stresses (τ_{max}) associated with pullout tests could be determined as in the following equations (e.g. Schlosser and Bastick, 1991; Abdelouhab et al., 2010):

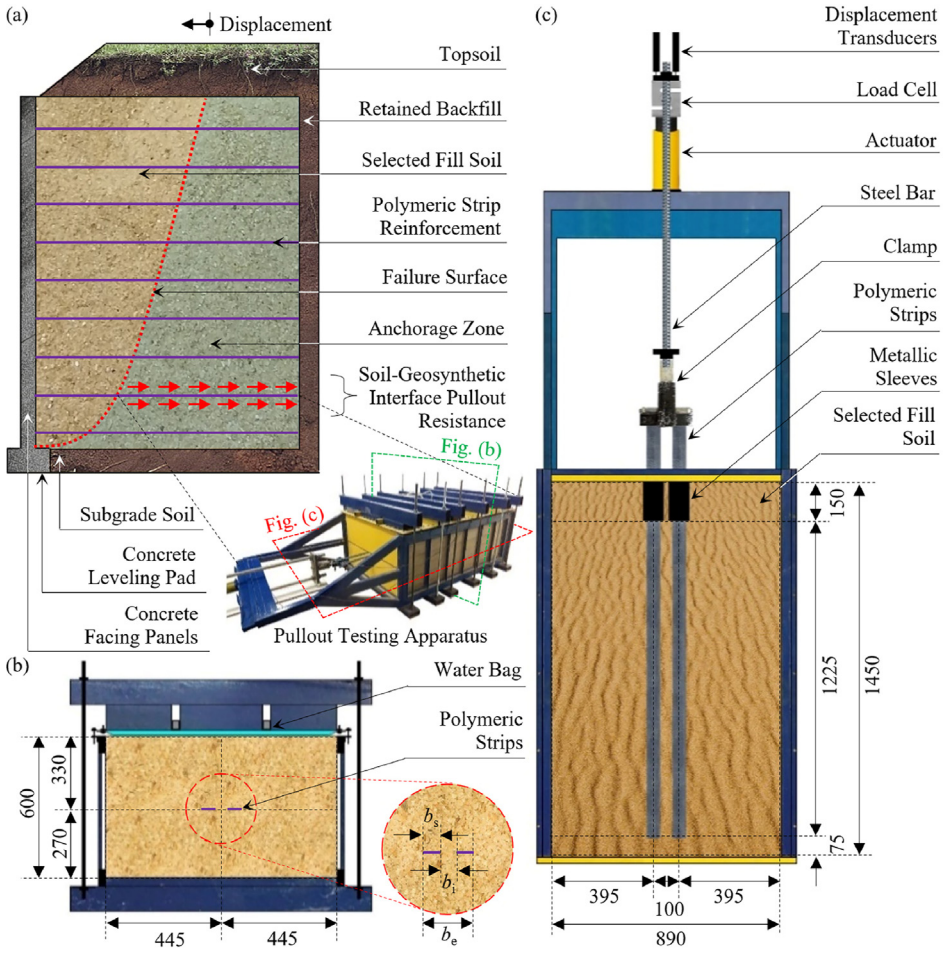

Fig. 11. Interface pullout resistance: (a) Schematic representation of the reinforced soil under working conditions and the laboratory pullout testing apparatus; (b) Vertical cross-section of pullout apparatus indicating strip geometry of installation; and (c) Top view of pullout apparatus on the reinforced horizontal plane. The dimensions are in mm.

$$\tau_{max} = \frac{P_{max}}{2L_g W_g} = f^* \sigma_{v,0} = f \sigma_{v,max} \tag{20}$$

where L_g is the reinforcement length, and W_g is the total reinforcement width, f^* is the apparent friction coefficient, and f is the actual friction coefficient.

Variables expressed in Eq. (20) may be rearranged to further evidence the relationship between $\sigma_{v,max}$, and $\sigma_{v,0}$:

$$\sigma_{v,max} = \frac{f^*}{f} \sigma_{v,0} \tag{21}$$

where f^*/f is assumed as a soil constant that facilitates correlations between geomechanical soil properties and the real stress configuration during pullout tests (Pierozan et al., 2022).

Pullout testing procedures are commonly employed in geotechnical engineering as they estimate design parameters, particularly the maximum pullout resistance (P_{max}). The following equation could be employed to provide a continuous sense of the values assumed by P_{max} in terms of the initial vertical stresses ($\sigma_{v,0}$), as it was developed and calibrated based on the experimental results (Pierozan et al., 2022):

$$P_{max} = k_1 + k_2 \sqrt{\sigma_{v,0} L_g W_g} \tag{22}$$

where k_1 and k_2 are the dimensionless fitted coefficients.

The apparent friction coefficients (f^*) are often the preferred design parameters as they do not rely on assumptions concerning the actual stress configuration under failure conditions ($\sigma_{v,max}$). The following relation is commonly utilized in this regard:

$$f^* = \frac{P_{max}}{2L_g W_g \sigma_{v,0}} \tag{23}$$

It should be noted that the theoretical assumptions and simplifications associated with f^* are inherently linked with more conservative designs, which could translate into low-cost efficiency. The consideration of variables depending on the actual stress configuration, such as when assuming f^*/f as a constant dependent on geomechanical soil properties and reinforcement characteristics, could partially fill the existing demand for more economic designs. Specifically, once the apparent friction coefficients (f^*) are experimentally determined, and the soil-reinforcement constant f^*/f is estimated based on laboratory tests or numerical analyses, the actual friction coefficients (f) may also be determined:

$$f = \frac{1}{\frac{f^*}{f}\frac{1}{f^*}} \tag{24}$$

Table 4
Summary of pullout test results.

Sample	Property	Test result		
		$\sigma_{v,0}$ = 12.5 kPa	$\sigma_{v,0}$ = 25 kPa	$\sigma_{v,0}$ = 50 kPa
S100-L0	$\delta_{face,max}$ (m)	0.29	0.36	0.46
	P_{max} (kN)	7.73	11.49	18.43
	$\sigma_{v,max}$ (kPa)	30.8	55.5	100.7
	$\Delta\sigma_{v,max}$ (kPa)	18.3	30.5	50.7
	f^*	2.52	1.88	1.5
	f	1.02	0.84	0.75
S50-L50	$\delta_{face,max}$ (m)	0.15	0.18	0.23
	P_{max} (kN)	4.37	5.88	7.48
	$\sigma_{v,max}$ (kPa)	21.4	35.4	61
	$\Delta\sigma_{v,max}$ (kPa)	8.9	10.4	11
	f^*	1.43	0.96	0.61
	f	0.83	0.68	0.5
S75-L25	$\delta_{face,max}$ (m)	0.19	0.23	0.28
	P_{max} (kN)	5.7	7.77	10.55
	$\sigma_{v,max}$ (kPa)	24.9	42.7	71.2
	$\Delta\sigma_{v,max}$ (kPa)	12.4	17.7	21.2
	f^*	1.86	1.27	0.86
	f	0.93	0.74	0.6
S0-L100	$\delta_{face,max}$ (m)	0.12	0.14	0.19
	P_{max} (kN)	2.58	3.57	5.07
	$\sigma_{v,max}$ (kPa)	15.7	31.1	57.3
	$\Delta\sigma_{v,max}$ (kPa)	3.2	6.1	7.3
	f^*	0.84	0.58	0.41
	f	0.67	0.47	0.36

Note: The soil samples used for pullout tests met the following compaction criteria: initial water content of approximately 0.25%, and relative density of 95% ± 3%, for sample S100-L0; and initial water content of w_{target} ± 2%, and relative compaction of 95% ± 3%, for samples S75-L25, S50-L50 and S0-L100. Since pullout tests were conducted in non-inundated conditions, water contents remained in the range of ±2%w_{target} before and after testing.

5.2. Impact of geomechanical soil properties

This section provides a discussion on the impact of geomechanical soil properties on variables used in the design of geosynthetic reinforced soil walls, i.e. f^* and f. The pullout test results that supported this evaluation are detailed in Pierozan et al. (2022), and the most relevant findings are summarized in Table 4.

The relationship between maximum pullout resistances (P_{max}) and initial vertical stresses ($\sigma_{v,0}$) is shown in Fig. 12a, along with the analytical approximation (Eq. (22)) that was employed in the range of 12.5–50 kPa to account for non-linearity between pullout resistance and vertical stresses. Tested values were also extrapolated for values of $\sigma_{v,0}$ in the range of 50–120 kPa. The values assumed by fitted coefficients k_1 and k_2 (Eq. (22)) are summarized in Table 3, along with additional relevant information. The apparent friction coefficients (f^*), as also represented in Fig. 12a, were determined based on data points according to pullout tests and considering the analytical approximation in the range of 12.5–120 kPa.

Detailed analysis of how the average values associated with vertical stresses acting on the reinforcements at failure conditions ($\sigma_{v,max}$) were determined is presented in Pierozan et al. (2022), and a summary of such variables are indicated in Table 4. Given the experimental results, Fig. 12b represents the relationship between $\sigma_{v,max,}$ and $\sigma_{v,0}$. Once the apparent friction coefficients (f^*) were calculated (Eq. (23)) in the range of 12.5–120 kPa, and considering the soil-reinforcement constants f^*/f (Table 3), it was possible to determine the actual friction coefficients (f) using Eq. (24). Parameters f^* and f are represented in terms of depth (z) and variables related to mineralogy and individual particles dimensions, i.e. SSR^{-1} and $FC_{particles}$, respectively, as shown in Fig. 12c.

Overall, based on the results shown in Fig. 12c, variables related to mineral composition (i.e. SSR^{-1}) and dimensions of individual soil particles (i.e. $FC_{particles}$) are directly correlated with pullout testing results. Differences between the surfaces representing parameters f^* and f (Fig. 12c) are indicative of considerable changes in stress distribution in the soil-reinforcement interface. Accordingly, these results suggest that variables such as SSR^{-1} and FC_{aggreg} could be implemented into design procedures of geosynthetic-reinforced soil walls to better capture the nuances of the geotechnical behavior, particularly when dealing with the sand-silt mixtures containing lateritic soils.

6. Conclusions

This paper investigated how the geomechanical performance of the sand-silt mixtures containing a lateritic soil, i.e. an intensely weathered tropical soil with the influence of interparticle bonding, is impacted by variables related to lateritic soil weathering. Nonetheless, the application of such non-conventional materials as structural fills in reinforced earth walls was also evaluated. The following conclusions can be drawn:

(1) The sesquioxide-silica ratio (SSR^{-1}) and the fines content relative to the individual particles ($FC_{particles}$) and the aggregations (FC_{aggreg}) directly correlated the soil geomechanical properties of the sand-silt mixtures containing lateritic soil, facilitating the delimitation of changes in geomechanical behavior due to the non-linearity observed between the variables.
(2) The sand-silt mixtures containing lateritic soil were considerably impacted by the changes in their internal structure as the relative proportion of fine-grained soil particles increased, i.e. from macro- and microstructural particle arrangement perspectives. Specifically, the bonding provided by the sesquioxides coating caused a significant decrease in the friction angles due to the decreased mobility of larger soil particles. Nonetheless, the fine-grained soil particles correlated with increased matric suction and restrained hydraulic conductivity capabilities relative to the coarser soil fractions.

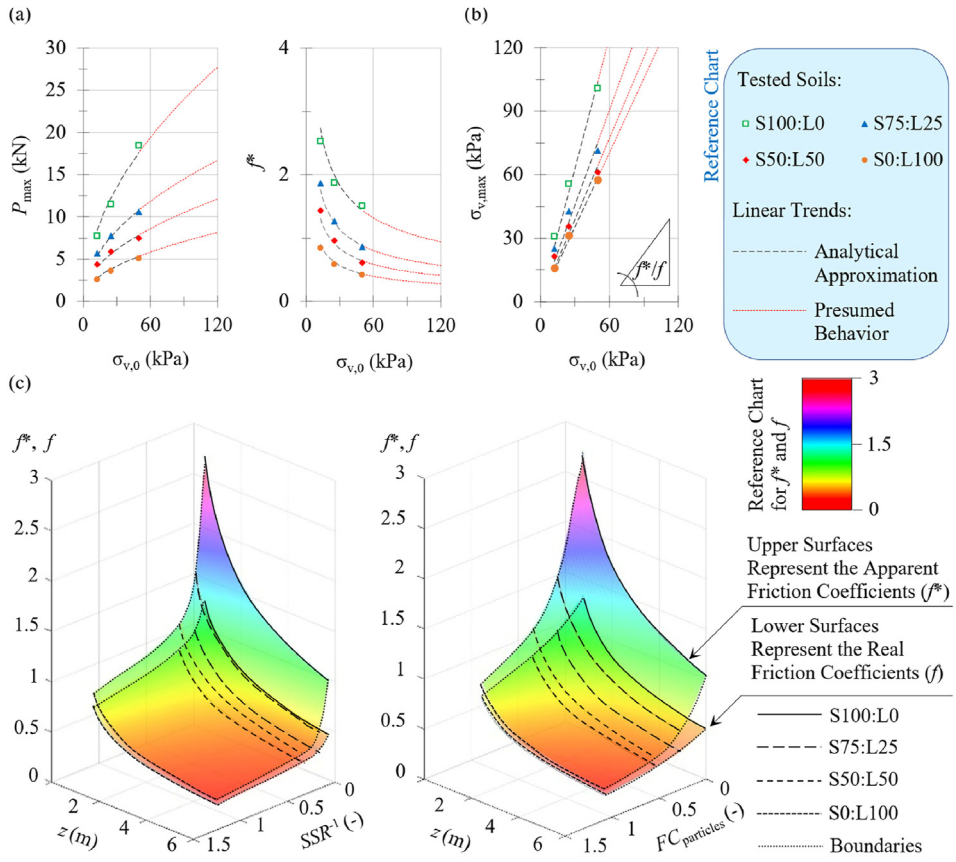

Fig. 12. Variables related to pullout tests: (a) Maximum pullout forces and corresponding apparent friction coefficients (f^*), (b) Relation between initial stress conditions ($\sigma_{v,0}$) and actual vertical stresses under failure conditions ($\sigma_{v,max}$), and (c) Impact of selected variables on the apparent and real friction coefficients (f^* and f, respectively).

(3) Soil packing was a factor of major relevance on the geomechanical behavior as it supported the delineation of boundaries associated with coarse- and fine-grained soil major influence, which could ultimately relate to the geomechanical responses presented in the sand-silt mixtures containing lateritic soils.
(4) The level of stresses mobilized on the soil-reinforcement interface during pullout tests could ultimately be associated with variables related to soil weathering, such as SSR^{-1} and FC_{aggreg}.

Overall, based on the results presented, it was observed that variables that denote the particularities of tropical soils, such as the sesquioxides-silica ratio (SSR^{-1}), and the fines content relative to the soil aggregations (FC_{aggreg}), could be implemented into design guidelines to further assist in anticipating the geomechanical behavior of silt-sand mixtures containing lateritic soils.

Declaration of competing interest

The authors declare that they have no known competing financial interests or personal relationships that could have appeared to influence the work reported in this paper.

Acknowledgments

The authors gratefully appreciate the funding provided by the Brazilian National Council for Scientific and Technological Development (CNPq), i.e. project number 471043/2013–3 (CNPq), the Coordination for the Improvement of Higher Education Personnel (CAPES), and the Federal District Research Foundation (FAP/DF) to conduct the various components of this research.

List of symbols

γ	Unit weight of soil (kN/m^3)
γ_d	Dry unit weight of soil (kN/m^3)
$\gamma_{d,max}$	Maximum dry unit weight of soil (kN/m^3)
$\gamma_{d,min}$	Minimum dry unit weight of soil (kN/m^3)
γ_b	Bulk unit weight of soil (kN/m^3)
$\gamma_{b,target}$	Target bulk unit weight of soil (kN/m^3)
$\gamma_{d,target}$	Target dry unit weight of soil (kN/m^3)
$\gamma_{n,target}$	Target unit weight of soil in their natural state (kN/m^3)
$\delta_{face,max}$	Face displacement under peak conditions (m)
δ_h	Horizontal shear displacement (m)
δ_v	Vertical shear displacement (m)
$\Delta\sigma_{v,max}$	Local stress increase under peak conditions (kPa)
θ_v	Volumetric water content
σ'_v	Effective vertical stress (kPa)
$\sigma_{v,0}$	Initial vertical stress (kPa)
$\sigma_{v,max}$	Vertical stress under peak conditions (kPa)
σ_w	Surface tension of water (N/m)
τ	Shear stress (kPa)
τ_{max}	Shear stress under peak conditions (kPa)
$\phi_{i,sec}$	Secant internal soil friction angle (inundated conditions)
$\phi_{ni,sec}$	Secant internal soil friction angle (non-inundated conditions)
Ψ	Angle of dilation (°)
a_1, a_2	Coefficients used in Eq. (4)
b_1, b_2	Coefficients used in Eq. (5)

b_e Distance between external boundaries of the strips (m)
b_i Distance between internal boundaries of the strips (m)
b_s Width of a single strip (m)
c_1, c_2 Coefficients used in Eq. (6)
$c_{Al_2O_3}$ Percentage of alumina
C_c Compression index
$c_{Fe_2O_3}$ Percentage of iron oxide
c_L Lateritic soil mass fraction
$c_{L,opt}$ Optimum lateritic soil mass fraction
C_r Recompression index
c_{SiO_2} Percentage of silica
C_{sw} Swelling index
c_S Host sand mass fraction
D Particle (or aggregation) dimension (m)
D_p Micro- or macro-pore diameter (m)
d_1, d_2 Coefficients used in Eqs. 11–13
e Void ratio
e_{B1}, e_{B2}, e_{B3} Void ratios referring to limit boundaries B1, B2 and B3, respectively
e_L Void ratio of the lateritic soil
e_{opt} Optimum void ratio
e_S Void ratio of the host sand
f Actual friction coefficient
f^* Apparent friction coefficient
$FC_{particles}$ Fines content relative to individual soil particles
FC_{aggreg} Fines content relative to water-stable soil aggregations
g_1, g_2 Coefficients used in Eq. (14)
G_s Specific gravity
h_1, h_2 Coefficients used in Eq. (15)
i_1, i_2 Coefficients used in Eq. (16)
j_1, j_2 Coefficients used in Eq. (18)
$k_{20\ °C}$ Hydraulic conductivity at 20 °C (m/s)
L_g Geosynthetic embedment (m)
m_L Dry mass of the lateritic soil (g)
m_S Dry mass of the host sand (g)
p_a Atmospheric pressure (kPa)
PI Plasticity index (dimensionless)
P_{max} Pullout resistance under peak conditions (kN)
P_{solids} Weight of solids (kN)
P_{total} Total weight of soil (kN)
P_{water} Weight of water (kN)
R^2 Coefficient of determination
S_a Specific surface area (m^2/g)
SSR Silica-sesquioxide ratio
SSR^{-1} Sesquioxide-silica ratio
u_a Pore-air pressure (kPa)
u_w Pore-water pressure (kPa)
v Volume fraction
v_{air} Volume fraction of air
v_{solids} Volume fraction of solids
v_{water} Volume fraction of water
V_{total} Total volume of soil (m^3)
V_{air} Volume of air (m^3)
V_{solids} Volume of solids (m^3)
V_{water} Volume of water (m^3)
w Water content
W_g Geosynthetic width considering a pair of strips (m)
w_L Liquid limit
w_{target} Target water content
w_{hig} Hygroscopic water content
w_{opt} Optimum water content
w_P Plastic limit

References

Abd, A.H., Utili, S., 2017. Design of geosynthetic-reinforced slopes in cohesive backfills. Geotext. Geomembranes 45 (6), 627–641.
Abdelouhab, A., Dias, D., Freitag, N., 2010. Physical and analytical modelling of geosynthetic strip pull-out behavior. Geotext. Geomembranes 28 (1), 44–53.
Abdi, M.R., Mirzaeifar, H., 2017. Experimental and PIV evaluation of grain size and distribution on soil-geogrid interactions in pullout test. Soils Found. 57 (6), 1045–1058.
Al Haj, K.M.A., Standing, J.R., 2016. Soil water retention curves representing two tropical clay soils from Sudan. Geotechnique 66 (1), 71–84.
Altay, G., Kayadelen, C., Taşkiran, T., Kaya, Y.Z., 2019. A laboratory study on pull-out resistance of geogrid in clay soil. Measurement 139 (1), 301–307.
Anggraini, V., Asadi, A., Syamsir, A., Huart, B.B.K., 2017. Three point bending flexural strength of cement treated tropical marine soil reinforced by lime treated natural fiber. Measurement 111 (1), 158–166.
Araujo, G.L.S., Palmeira, E.M., Cunha, R.P., 2009. Behaviour of geosynthetic-encased granular columns in porous collapsible soil. Geosynth. Int. 16 (6), 433–451.
Araujo, G.L.S., Moreno, J.A.S., Zornberg, J.G., 2021. Shear behavior of mixtures involving tropical soils and tire shreds. Construct. Build. Mater. 276 (4), 122061.
Arnepalli, D.N., Shanthakumar, S., Rao, B.H., Singh, D.N., 2008. Comparison of methods for determining specific-surface area of fine-grained soils. Geotech. Geol. Eng. 26 (2), 121–132.
ASTM D421-85, 2007. Standard Practice for Dry Preparation of Soil Samples for Particle-Size Analysis and Determination of Soil Constants. ASTM International, West Conshohocken, PA, USA.
ASTM D422-63e2, 2007. Standard Test Method for Particle-Size Analysis of Soils. ASTM International, West Conshohocken, PA, USA.
ASTM D3080/D3080M-11, 2011. Standard Test Method for Direct Shear Test of Soils under Consolidated Drained Conditions. ASTM International, West Conshohocken, PA, USA.
ASTM D6706-01, 2013. Standard Test Method for Measuring Geosynthetic Pullout Resistance in Soil. ASTM International, West Conshohocken, PA, USA.
ASTM D854-14, 2014. Standard Test Method for Specific Gravity of Soil Solids by Water Pycnometer. ASTM International, West Conshohocken, PA, USA.
ASTM D4253-16e1, 2016. Standard Test Methods for Maximum Index Density and Unit Weight of Soils Using a Vibratory Table. ASTM International, West Conshohocken, PA, USA.
ASTM D4254-16, 2016. Standard Test Methods for Minimum Index Density and Unit Weight of Soils and Calculation of Relative Density. ASTM International, West Conshohocken, PA, USA.
ASTM D5084-16a, 2016. Standard Test Methods for Measurement of Hydraulic Conductivity of Saturated Porous Materials Using a Flexible Wall Permeameter. ASTM International, West Conshohocken, PA, USA.
ASTM D5298-16, 2016. Standard Test Method for Measurement of Soil Potential (Suction) Using Filter Paper. ASTM International, West Conshohocken, PA, USA.
ASTM D4287-17e1, 2017. Standard Practice for Classification of Soils for Engineering Purposes (Unified Soil Classification System). ASTM International, West Conshohocken, PA, USA.
ASTM D4318-17e1, 2017. Standard Test Methods for Liquid Limit, Plastic Limit, and Plasticity Index of Soils. ASTM International, West Conshohocken, PA, USA.
ASTM D4221-18, 2018. Standard Test Method for Dispersive Characteristics of Clay Soil by Double Hydrometer. ASTM International, West Conshohocken, PA, USA.
ASTM D2434-19, 2019. Standard Test Method for Permeability of Granular Soils (Constant Head). ASTM International, West Conshohocken, PA, USA.
ASTM D2435/D2435M-11, 2020. Standard Test Methods for One-Dimensional Consolidation Properties of Soils Using Incremental Loading. ASTM International, West Conshohocken, PA, USA.
ASTM D698-12, 2021. Standard Test Methods for Laboratory Compaction Characteristics of Soil Using Standard Effort (12,400 Ft-Lbf/ft^3 (600 kN-M/m^3)). ASTM International, West Conshohocken, PA, USA.
Benatti, J.C.B., Miguel, M.G., 2013. A proposal of structural models for colluvial and lateritic soil profile from southwestern Brazil on the basis of their collapsible behavior. Eng. Geol. 153 (1), 1–11.
Berg, R., Christopher, B., Samtani, N., 2009. Design and Construction of Mechanically Stabilized Earth Walls and Reinforced Soil Slopes –, ume I. U.S. Department of Transportation, Federal Highway Administration, Washington, DC, USA.
Brunauer, S., Emmett, P.H., Teller, E., 1938. Adsorption of gases in multimolecular layers. J. Am. Chem. Soc. 60 (2), 309–319.
BS EN 14475, 2006. Execution of Special Geotechnical Works – Reinforced Fill. British Standards Institution, London, United Kingdom.
Carvalho, J.C., Rezende, L.R., Cardoso, F.B.F., Lucena, L.C.F.L., Guimarães, R.C., Valencia, Y.G., 2015. Tropical soils for highway construction: peculiarities and considerations. Transp. Geotech. 5 (1), 3–19.
Catt, J.A., 1990. Tropical residual soils geological society engineering group working party report. Q. J. Eng. Geol. Hydrogeol. 23 (1), 4–101.
Chang, C.S., Yin, Z.-Y., 2011. Micromechanical modeling for behavior of silty sand with influence of fine content. Int. J. Solid Struct. 48 (15), 2655–2667.
Chang, C.S., Wang, J.-Y., Ge, L., 2015. Modeling of minimum void ratio for sand-silt mixtures. Eng. Geol. 196 (1), 293–304.
Chen, Y., Gao, Y., Yang, S., Zhang, F., 2018. Required unfactored geosynthetic strength of three-dimensional reinforced soil structures comprised of cohesive backfills. Geotext. Geomembranes 46 (6), 860–868.

EBGEO, 2011. Recommendations for Design and Analysis of Earth Structures Using Geosynthetic Reinforcements, second ed. Ernt & Sohn, Berlin, Germany.
Elias, V., Christopher, B.R., Berg, R.R., 2001. Mechanically Stabilized Earth Walls and Reinforced Soil Slopes: Design and Construction Guidelines. U.S. Department of Transportation, Federal Highway Administration, Washington, DC, USA.
Freitas, J.B. de, Rezende, L.B. de, Gitirana Junior, de F.N, G., 2020. Prediction of the resilient modulus of two tropical subgrade soils considering unsaturated conditions. Eng. Geol. 270 (1), 105580.
Gidigasu, M.D., 1972. Mode of formation and geotechnical characteristics of laterite materials of Ghana in relation to soil forming factors. Eng. Geol. 6 (2), 79–150.
Guimarães, A.C.R., Silva Filho, J.C., Castro, C.D., 2021. Contribution to the use of alternative material in heavy haul railway sub-ballast layer. Transp. Geotech. 30 (1), 100524.
Jewell, R.A., 1989. Direct shear tests on sands. Geotechnique 39 (2), 309–322.
Klein, C., Hurlbut, C.S., 1993. Manual of Mineralogy (After James D. Dana), twenty-first ed. John Wiley & Sons, NY, USA.
Kido, R., Kimura, M., 2021. Investigation of soil deformation characteristics during pullout of a ribbed reinforcement using X-ray micro CT. Soils Found. 61 (3), 642–657.
Lajevardi, S.H., Dias, D., Racinais, J., 2013. Analysis of soil-welded steel mesh reinforcement interface interaction by pull-out tests. Geotext. Geomembranes 40 (1), 48–57.
Latifi, N., Rashid, A.S.A., Siddiqua, S., Majid, M.Z.A., 2016. Strength measurement and textural characteristics of tropical residual soil stabilized with liquid polymer. Measurement 91 (1), 46–54.
Latifi, N., Eisazadeh, A., Marto, A., Meehan, C.L., 2017. Tropical residual soil stabilization, a powder form material for increasing soil strength. Construct. Build. Mater. 147 (1), 827–836.
Leroueil, S., Vaughan, P.R., 1990. The general and congruent effects of structure in natural soils and weak rocks. Geotechnique 40 (3), 467–488.
Lima, C.D.A., Motta, L.M.G., Aragão, F.T.S., 2021. A permanent deformation predictive model for fine tropical soils considering the effects of the compaction moisture content on material selection. Transp. Geotech. 28 (1), 100534.
Mahalinga-Iyer, Y., Williams, D.J., 1994. Consolidation and shear strength properties of a lateritic soil. Eng. Geol. 38 (1–2), 53–63.
Mengue, E., Mroueh, H., Lancelot, L., Eko, R.M., 2018. Design and parametric study of a pavement foundation layer made of cement-treated fine-grained lateritic soil. Soils Found. 58 (3), 666–677.
Mitchell, J.K., Soga, K., 2005. Fundamentals of Soil Behavior, third ed. Wiley, Hoboken, NJ, USA.
Miyata, Y., Bathurst, R.J., Allen, T.M., 2019. Calibration of PET strap pullout models using a statistical approach. Geosynth. Int. 26 (4), 413–427.
Mohamed, A.-M.O., Paleologos, E.K., 2018. Hydraulic properties of soils. In: Mohamed, A.-M.O., Paleologos, E.K. (Eds.), Fundamentals of Geoenvironmental Engineering. Butterworth-Heinemann, Oxford, United Kingdom, pp. 459–495.
Morandini, T.L.C., Leite, A. do L., 2015. Characterization of hydraulic conductivity of tropical soils and bentonite mixtures for CCL purposes. Eng. Geol. 196 (1), 251–267.
NF P94-270, 2009. Geotechnical Design – Retaining Structures – Reinforced and Soil Nailing Structures. Association Française de Normalisation, Paris, France (in French).
Ng, C.W.W., Akinniyi, D.B., Zhou, C., Chiu, C.F., 2019. Comparisons of weathered lateritic, granitic and volcanic soils: compressibility and shear strength. Eng. Geol. 24 (1), 235–240.
Okagbue, C.O., Onyeobi, T.U.S., 1999. Potential of marble dust to stabilize red tropical soils for road construction. Eng. Geol. 53 (3–4), 371–380.
Palmeira, E.M., 1996. Design and construction of a large-scale pullout box (in Portuguese). In: Research Report. University of Brasilia, Federal District, Brazil.
Palmeira, E.M., 2004. Bearing force mobilization in pull-out tests on geogrids. Geotext. Geomembranes 22 (6), 481–509.
Palmeira, E.M., 2009. Soil-geosynthetic interaction: modelling and analysis. Geotext. Geomembranes 27 (5), 368–390.
Pierozan, R.C., 2018. Interface resistance of metallic and polymeric strips embedded in different soils (in Portuguese). In: PhD Thesis. University of Brasilia, Federal District, Brazil.
Pierozan, R.C., Araujo, G.L.S., Palmeira, E.M., Romanel, C., Zornberg, J.G., 2022. Interface pullout resistance of polymeric strips embedded in marginal tropical soils. Geotext. Geomembranes 50 (1), 20–39.
Portelinha, F.H.M., Santos, M.C., Futai, M.M., 2021. A laboratory evaluation of reinforcement loads induced by rainfall infiltration in geosynthetic mechanically stabilized earth walls. Geotext. Geomembranes 49 (5), 1427–1439.
Rezende, L.R., Camapum-de-Carvalho, J., Palmeira, E.M., 2015. The use of alternative and improved construction materials and geosynthetics for pavements. In: Indraratna, B., Chu, J., Rujikiatkamjorn, C. (Eds.), Ground Improvement – Case Histories. Elsevier Geo-Engineering Book Series, Amsterdam, Netherlands, pp. 481–505.
Riccio, M., Ehrlich, M., Dias, D., 2014. Field monitoring and analyses of the response of a block-faced geogrid wall using fine-grained tropical soils. Geotext. Geomembranes 42 (2), 127–138.
Santos, E.C.G., Palmeira, E.M., Bathurst, R.J., 2013. Behaviour of geogrid reinforced wall built with recycled construction and demolition waste backfill on a collapsible foundation. Geotext. Geomembranes 39 (1), 9–19.
Schanz, T., Vermeer, P.A., 1996. Angles of friction and dilatancy of sand. Geotechnique 46 (1), 145–151.
Schlosser, F., Bastick, M., 1991. Reinforced earth. In: Fang, H.Y. (Ed.), Foundation Engineering Handbook. Springer, Boston, USA, pp. 778–795.
Shackelford, C.D., 2013. Geoenvironmental Engineering – Reference Module in Earth Systems and Environmental Sciences, first ed. Elsevier, Amsterdam, Netherlands.
Silva, M.F., Ribeiro, M.M.P., Furlan, A.P., Fabbri, G.T.P., 2021. Effect of compaction water content and stress ratio on permanent deformation of a subgrade lateritic soil. Transp. Geotech. 26 (1), 100443.
Simoni, A., Houlsby, G.T., 2006. The direct shear strength and dilatancy of sand-gravel mixtures. Geotech. Geol. Eng. 24 (3), 523–549.
Townsend, F.C., Manke, P.G., Parcher, J.V., 1971. The influence of sesquioxides on lateritic soil properties. Transport. Res. Rec. 374 (1), 80–92.
Tran, T.V., Alkema, D., Hack, R., 2019. Weathering and deterioration of geotechnical properties in time of groundmasses in a tropical climate. Eng. Geol. 260 (1), 105221.
Xenaki, V.C., Athanasopoulos, G.A., 2003. Liquefaction resistance of sand-silt mixtures: an experimental investigation on the effect of fines. Soil Dynam. Earthq. Eng. 23 (3), 1–12.
Xiao, C., Gao, S., Liu, H., Du, Y., 2021. Case history on failure of geosynthetics-reinforced soil bridge approach retaining walls. Geotext. Geomembranes 49 (6), 1585–1599.
Yang, S.L., Sandven, R., Grande, L., 2006. Instability of sand-silt mixtures. Soil Dynam. Earthq. Eng. 26 (2–4), 183–190.
Yin, Z.-Y., Zhao, J., Hicher, P.-Y., 2014. A micromechanics-based model for sand-silt mixtures. Int. J. Solid Struct. 51 (6), 1350–1363.
Yin, Z.-Y., Huang, H.-W., Hicher, P.-Y., 2016. Elastoplastic modeling of sand-silt mixtures. Soils Found. 56 (3), 520–532.
Zhang, L.M., Li, X., 2010. Microporosity structure of coarse granular soils. J. Geotech. Geoenviron. Eng. 136 (10), 1425–1436.
Zhang, X., Baudet, B.A., Yao, T., 2020. The influence of particle shape and mineralogy on the particle strength, breakage and compressibility. Int. J. Geotech. Eng. 11, 1.

Rodrigo Cesar Pierozan earned his BSc and MSc degrees in Civil Engineering from the Federal University of Paraná, Brazil in 2012 and 2014, respectively, and his PhD in Geotechnics from the University of Brasília, Brazil in 2018. He served as a postdoctoral research fellow at the University of Texas at Austin in 2019 and subsequently held the same position at the Pontifical Catholic University of Rio de Janeiro, Brazil from 2020 to 2022. Currently, he is a professor in the Department of Civil Engineering at the Federal Institute of Education, Science, and Technology of Rondônia, Brazil, where he teaches courses related to geotechnical engineering and transportation and conducts research in these areas. His research interests include (1) evaluating the specific behavior of tropical soils in infrastructure projects, (2) studying the use of geosynthetics in transportation infrastructure and hydraulic works, and (3) assessing the use of alternative and sustainable materials in Geotechnics. He strives to expand the horizons of teaching through research and innovation.